J. Am. Chem. Soc. **2021**, *143*, *49*, 20645-20656

https://pubs.acs.org/doi/abs/10.1021/jacs.1c06429

Reduction of Electron Repulsion in Highly Covalent Fe-Amido Complexes Counteracts the Impact of a Weak Ligand Field on Excited-State Ordering

Christopher B. Larsen,[a†] Jason D. Braun,[b†] Issiah B. Lozada, [b†] Kristjan Kunnus,[a] Elisa Biasin, [a] Charles Kolodziej,[c] Clemens Burda,[c] Amy A. Cordones, [a] Kelly J. Gaffney [a]* and David E. Herbert[b]**

[a] Stanford PULSE Institute, SLAC National Accelerator Laboratory, Stanford University, 2575 Sand Hill Road, Menlo Park, CA 94025, USA; *acordon@slac.stanford.edu, *kgaffney@slac.stanford.edu

[b] Department of Chemistry and the Manitoba Institute for Materials, University of Manitoba, 144 Dysart Rd, Winnipeg, MB, R3T 2N2, Canada; *david.herbert@umanitoba.ca

[c] Department of Chemistry, Case Western Reserve University, 10900 Euclid Ave, Cleveland, OH, 44106, USA

[†] These authors contributed equally to this work.

ABSTRACT

The ability to access panchromatic absorption and long-lived charge-transfer (CT) excited states is critical to the pursuit of abundant-metal molecular photosensitizers. Fe(II) complexes supported by benzannulated diarylamido ligands have been reported to broadly absorb visible light with nanosecond CT excited state lifetimes, but as amido donors exert a weak ligand field, this defies conventional photosensitizer design principles. Here, we report an aerobically stable Fe(II) complex of a phenanthridine/quinoline diarylamido ligand, Fe(^{Cl}**L**)$_2$, with panchromatic absorption and a 3 ns excited-state lifetime. Using X-ray absorption spectroscopy (XAS) and resonant inelastic X-ray scattering (RIXS) at the Fe L-edge and N K-edge, we experimentally validate the strong Fe-N_{amido} orbital mixing in Fe(^{Cl}**L**)$_2$ responsible for the panchromatic absorption and demonstrate a previously unreported competition between ligand-field strength and metal-ligand (Fe-N_{amido}) covalency that stabilizes the ^{3}CT state over the lowest energy triplet metal-centered (^{3}MC) state in the ground-state geometry. Single-crystal X-ray diffraction (XRD) and density functional theory (DFT) suggest formation of this CT state depopulates an orbital with Fe-N_{amido} antibonding character, causing metal-ligand bonds to contract and accentuating the geometric differences between CT and MC excited states. These effects diminish the driving force for electron transfer to metal-centered excited states and increase the intramolecular reorganization energy, critical properties for extending the lifetime of CT excited states. These findings highlight metal-ligand covalency as a novel design principle for elongating excited state lifetimes in abundant metal photosensitizers.

INTRODUCTION

The most effective molecular photosensitizers for photocatalytic[1] and photovoltaic[2] applications broadly absorb visible light[3,4] and exhibit suitably long-lived charge-transfer (CT) excited states for efficient charge injection into semiconductor surfaces[5] or amassing sufficient concentrations of reactive excited states for synthesis.[6] Coordination complexes of precious metals in low-oxidation states such as Ru(II) or Ir(III) with chelating, π-acceptor ligands can fulfill these criteria effectively, but cost and scarcity considerations have driven the search for chromophores based on more abundant materials that do not compromise on performance.[7,8] While creative ligand designs have enabled the development of an increasing number of exciting candidates based on Cu,[9,10] Zr,[11–14] Co[15,16] and Cr,[17–19] iron has long represented a key target in this area.[7] The realization of useful Fe(II)-based photosensitizers, however, has been stymied by the inherent tendency of first-row transition metal complexes to undergo rapid deactivation of CT excited-states via lower-lying metal-centered (MC) states.[20] Thus, while $[Ru(bpy)_3]^{2+}$ (bpy = 2,2'-bipyridine) luminesces from a metal-to-ligand charge-transfer (^{3}MLCT) excited state with a lifetime of *ca.* 900 ns,[21] the same state in the homologous, isoelectronic complex $[Fe(bpy)_3]^{2+}$ deactivates to the MC manifold on a sub-picosecond timescale.[22,23] The positioning of low-lying MC states in Fe(II) complexes are a consequence of the weaker ligand fields that result from the 'primogenic effect',[24,25] in which the contracted nature of the 3d orbitals of first-row transition metal complexes leads to weakened metal-ligand bonding and enhanced electron-electron repulsion in the d subshell, stabilizing MC states relative to CT ones.[26]

Efforts to identify strategies by which electron transfer from CT to MC states can be suppressed have consequently focused to a large extent on manipulating the energy difference between these states through ligand design.[20] Two approaches presently dominate: (1)

destabilizing MC states by increasing the ligand-field strength (Figure 1, red arrow); or (2) decreasing the energy of the CT state (Figure 1, blue arrow). The most promising example of the first approach has been the incorporation of strongly σ-donating *N*-heterocyclic (NHC) and mesoionic carbene donors into ligand scaffolds.[27] At the saturation limit of six carbenes arranged octahedrally around an Fe(II) ion, the $^3T_{1g}$ state was raised sufficiently for a 528 ps ^{3}MLCT lifetime to be observed.[28] However, a collateral consequence of the enhanced electron density at the iron center due to the presence of such strongly σ-donating ligands was a shift in the Fe(II/III) redox couple to negative potentials, resulting in ferric congeners being favored under aerobic conditions.[29] Such Fe(III) complexes can exhibit nanosecond excited states, but with spin-allowed ligand-to-metal charge transfer (^{2}LMCT) character.[30] With respect to the second strategy, ^{3}MLCT excited states have been stabilized in $[Fe(CN)_4(bpy)]^{2-}$ and related complexes[31,32] by decreasing the ligand acceptor orbital energy.[33] As the ^{3}MLCT energy is lowered below that of the nominally $^3T_{1g}$ state, its lifetime increases due to a higher activation barrier for electron transfer between CT and MC states. Despite these and other[34,35] conceptual successes, the charge-transfer lifetimes of Fe(II) photosensitizer candidates have remained firmly in the ps regime.

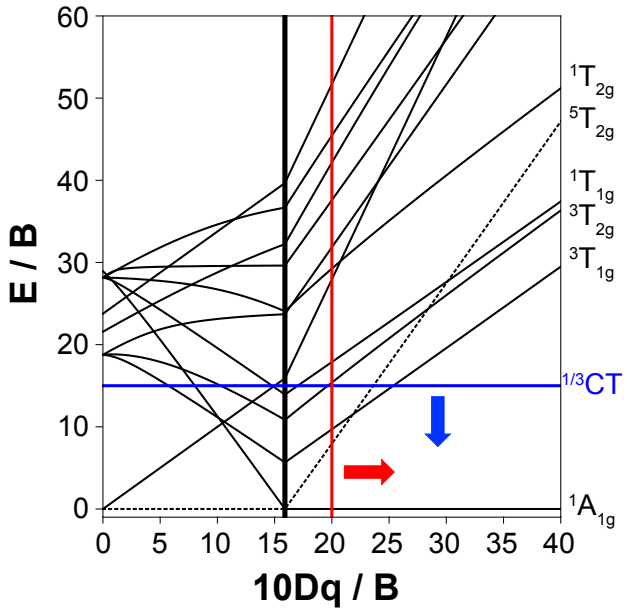

Figure 1. Partial Tanabe-Sugano diagram for a d^6 Fe(II) ion. The arrows depict the two main approaches for stabilizing CT excited-states over MC ones: red = increasing ligand-field strength, blue = decreasing CT state energy.

A distinct approach is to increase mixing between filled metal t_{2g} orbitals and filled ligand molecular orbitals, as highlighted by a computational investigation of pseudo-octahedral complexes of 2,2':6',2"-terpyridine (terpy) ligands with adjustable π-donor properties (i.e., $[Fe(terpy)_2]^{2+}$; Figure 2a).[36] In this way, the character of the highest occupied molecular orbital (HOMO) can be transformed from metal- to ligand-centered in a process termed 'HOMO inversion'. In addition to increasing the HOMO energy, such mixing was predicted to foster multiple, mixed metal-to-ligand and intraligand charge transfer (MLCT/ILCT) transitions in the visible region, broadening the overall absorption envelope in regions of relevance to solar energy harvesting. We recently reported the construction of pseudo-octahedral Fe(II) complexes, $Fe(^{R}\mathbf{L})_2$ (R = *t*Bu, CF_3), where $^{R}\mathbf{L}$ is a benzannulated pincer-type (4-phenanthridinyl)(8-quinolinyl)amido ligand (Figure 2b).[37] Such complexes indeed have broad absorptive cross-sections across the visible spectrum ($\varepsilon > 5000$ M^{-1} cm^{-1} from $\lambda = 250 - 795$ nm) and exhibit nanosecond excited-state

lifetimes assigned to charge-transfer (CT) states using a combination of transient absorption spectroscopy and spectroelectrochemistry. Fe(^{R}**L**)$_2$ can be thought of as an intermediate case of HOMO inversion where the energies of the HOMO through to HOMO-4 are spread out by strong mixing between Fe 3d and amido-based N 2p orbitals. Similar mixing is absent from other first-row transition and main-group metal complexes (e.g., M = Ga; Figure 2c) in which the HOMO becomes wholly ligand centered.[38]

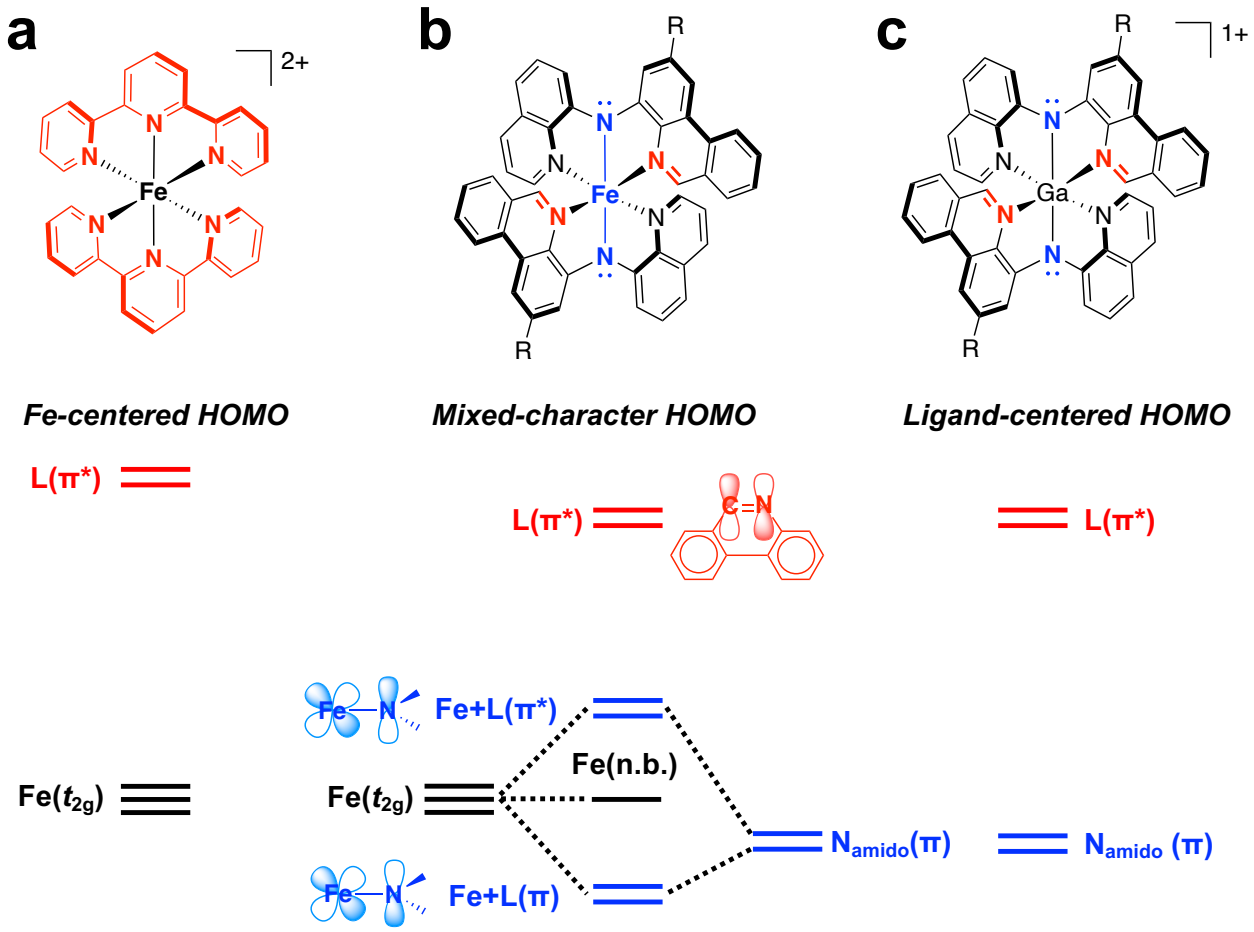

Figure 2. Structures and abbreviated frontier orbital energy level diagrams for (a) $[Fe(terpy)_2]^{2+}$, (b) Fe(^{R}**L**)$_2$ and (c) $[Ga(^{R}\mathbf{L})_2]^{+}$.

From ligand field theory, such orbital mixing is expected for complexes of weak-field π-donors like diarlyamido ligands.[39] However, the same level of theory[20] predicts that this mixing

should lower the octahedral splitting energy (10Dq) and stabilize metal-centered (MC) states relative to CT ones (equivalent to shifting the red vertical line in Figure 1 back to the left) providing an efficient excited state decay channel. Yet, the absorption features of Fe(^{R}**L**)$_2$ assigned to a CT excited state persist for nanoseconds.[37] We therefore set out to understand why strong Fe-N$_{amido}$ metal-ligand orbital mixing should supersede the impact of the anticipated decrease in ligand field. To do so, we constructed an aerobically stable, panchromatic absorbing Fe(^{R}**L**)$_2$ complex (R = Cl) that exhibits a multi-nanosecond excited state lifetime and investigated its electronic structure and excited-state ordering using X-ray absorption spectroscopy (XAS) and resonance inelastic X-ray scattering (RIXS) at the Fe L$_3$-edge and N K-edge. To isolate the impact of the mixed-character HOMO anticipated for Fe(^{Cl}**L**)$_2$, [Fe(^{Cl}**L**)$_2$][PF$_6$], [Ga(^{Cl}**L**)$_2$][PF$_6$] and [Fe(terpy)$_2$][PF$_6$]$_2$ were also included for study. The one-electron oxidized [Fe(^{Cl}**L**)$_2$][PF$_6$] was chosen to serve as a proxy for the electronic structure of Fe in the CT excited state.[40] [Ga(^{Cl}**L**)$_2$][PF$_6$] and [Fe(terpy)$_2$][PF$_6$]$_2$ were selected as controls for identifying which N and Fe spectral features, respectively, are specifically associated with Fe-N$_{amido}$ covalency. The Ga(III) center in [Ga(^{Cl}**L**)$_2$][PF$_6$] has a fully occupied 3d sub-shell whose orbitals do not mix with those of the ligand, such that the main-group metal ion acts as a structural scaffold to orient the ligands in the same orientation as Fe(^{Cl}**L**)$_2$ but without metal-ligand orbital hybridization;[38] [Fe(terpy)$_2$][PF$_6$]$_2$ lacks the amido functionality entirely. By selecting either Fe 2p or N 1s resonances, our XAS measurements access the unoccupied frontier orbitals, while our RIXS measurements assess valence electronic excited states from both the metal and ligand perspective, and with atomic specificity. This has enabled us to experimentally validate strong metal-ligand orbital mixing in this new class of Fe(II) photosensitizer and demonstrate a hitherto unreported competition between decreasing 10Dq (due to weaker field π-donor ligands) and decreasing electron-electron repulsion in the Fe 3d orbitals (due to strong metal-ligand orbital

mixing), highlighting metal-ligand covalency as a molecular design principle for accessing long-lived charge-transfer excited states.

RESULTS AND DISCUSSION

Synthesis and Characterization

In our previous study of Fe(II) complexes of diarylamido ligands bearing π-extended phenanthridine (benzo[*c*]quinoline) units, Fe($^{\mathbf{R}}$**L**)$_2$, we found that while placing strongly electron withdrawing CF_3 groups in the 2-position of the phenanthridinyl moieties ($^{\mathbf{CF3}}$**L**, R = CF_3) anodically shifted the [Fe($^{\mathbf{R}}$**L**)$_2$]$^{0/+}$ redox couple by ~200 mV compared with a *t*Bu-substituted variant ($^{\mathbf{tBu}}$**L**), Fe($^{\mathbf{CF3}}$**L**)$_2$ oxidizes in aerated solutions to the cationic [Fe($^{\mathbf{CF3}}$**L**)$_2$]$^+$.[37] After surveying a number of substituents, we found that, in comparison, analogs bearing a 2-chlorophenanthridinyl unit ($^{\mathbf{Cl}}$**L**)[41] show much improved stability in air (see Figures S1-S2, Table S1 and discussion in Supporting Information, p. SI-18). The neutral pseudo-octahedral Fe(II) complex, Fe($^{\mathbf{Cl}}$**L**)$_2$, could be accessed in two ways: directly from a ferrous salt (Fe(OTf)$_2$; OTf = trifluoromethylsulfonate) and NaO*t*Bu in THF at room temperature, or via chemical reduction of [Fe($^{\mathbf{Cl}}$**L**)$_2$][PF_6] using a suitable reducing agent such as cobaltocene (Scheme 1). The diamagnetic Fe(II) complex Fe($^{\mathbf{Cl}}$**L**)$_2$ is soluble in common organic solvents with NMR spectroscopic features consistent with installation of two equivalents of $^{\mathbf{Cl}}$**L** on Fe. The cation in [Fe($^{\mathbf{Cl}}$**L**)$_2$][PF_6] is best described as a S = ½ paramagnet with broad peaks spanning from δ = -70 – 30 ppm in the ^{1}H NMR spectrum and a solution magnetic moment μ_{eff} = 1.31 determined via Evans' method. [Ga($^{\mathbf{Cl}}$**L**)$_2$][PF_6] was prepared in a similar fashion from $GaCl_3$ in THF.

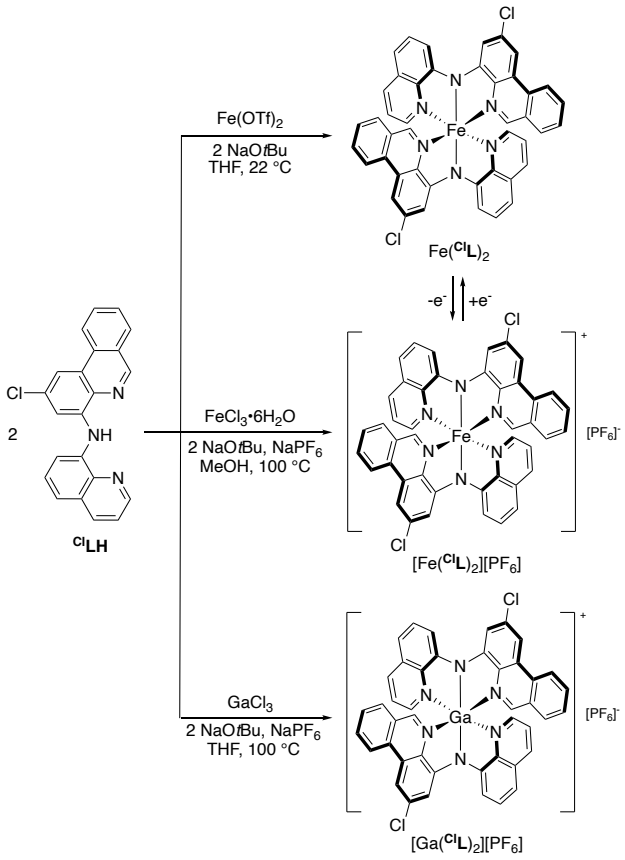

Scheme 1. Synthesis of *bis*((2-chloro-4-phenanthridinyl)(8-quinolinyl)amido)) complexes Fe(^{Cl}**L**)$_2$, [Fe(^{Cl}**L**)$_2$][PF$_6$] and [Ga(^{Cl}**L**)$_2$][PF$_6$].

For X-ray spectroscopic measurements, it is important to understand the consequences of geometry on molecular orbitals (MOs). Pseudo-octahedral complexes bearing two ^{Cl}**L** ligands formally possess D_{4h} symmetry from the perspective of the metal, whereas [Fe(terpy)$_2$](PF$_6$)$_2$ is C_{2v} symmetric. In ligand field theory, D_{4h} descent from octahedral (O_h) symmetry splits the triply degenerate t_{2g} orbital set into b_{2g} and e_g orbitals, the latter of which mix with e_g ligand-grouped orbitals (LGOs) of appropriate energy in Fe(^{Cl}**L**)$_2$ and [Fe(^{Cl}**L**)$_2$][PF$_6$] to form π-bonding and anti-bonding MOs with e_g symmetry (labelled Fe+L(π) and Fe+L(π*) in Figure 2b). The b_{2g} orbital does not have appropriate symmetry to mix with the amido LGOs (a_{1g}, e_g, a_{2u} and e_u) and is consequently non-bonding with respect to the amido groups (labelled Fe(n.b.) in Figure 2b).

Furthermore, the O_h e_g orbital set splits into b_{1g} and a_{1g} orbitals. This first-principles description of metal-ligand bonding is supported by DFT calculations which corroborate the mixed character of the occupied frontier orbitals of $[Fe(^{Cl}L)_2]^{0/+}$ and identify the b_{1g} and a_{1g} unoccupied MOs of $d_{x^2-y^2}$ and d_{z^2} parentage as the LUMO+10 and LUMO+11, respectively, for $Fe(^{Cl}L)_2$ (Figure 3; see also Tables S2-S5 and Figures S3-S6 and Supporting Information p. SI-15-16 for a discussion of the choice of functional). In comparison, both the degenerate HOMO and HOMO-1 for $[Ga(^{Cl}L)_2]^+$ have dominant N_{amido} character with no contribution from the metal.

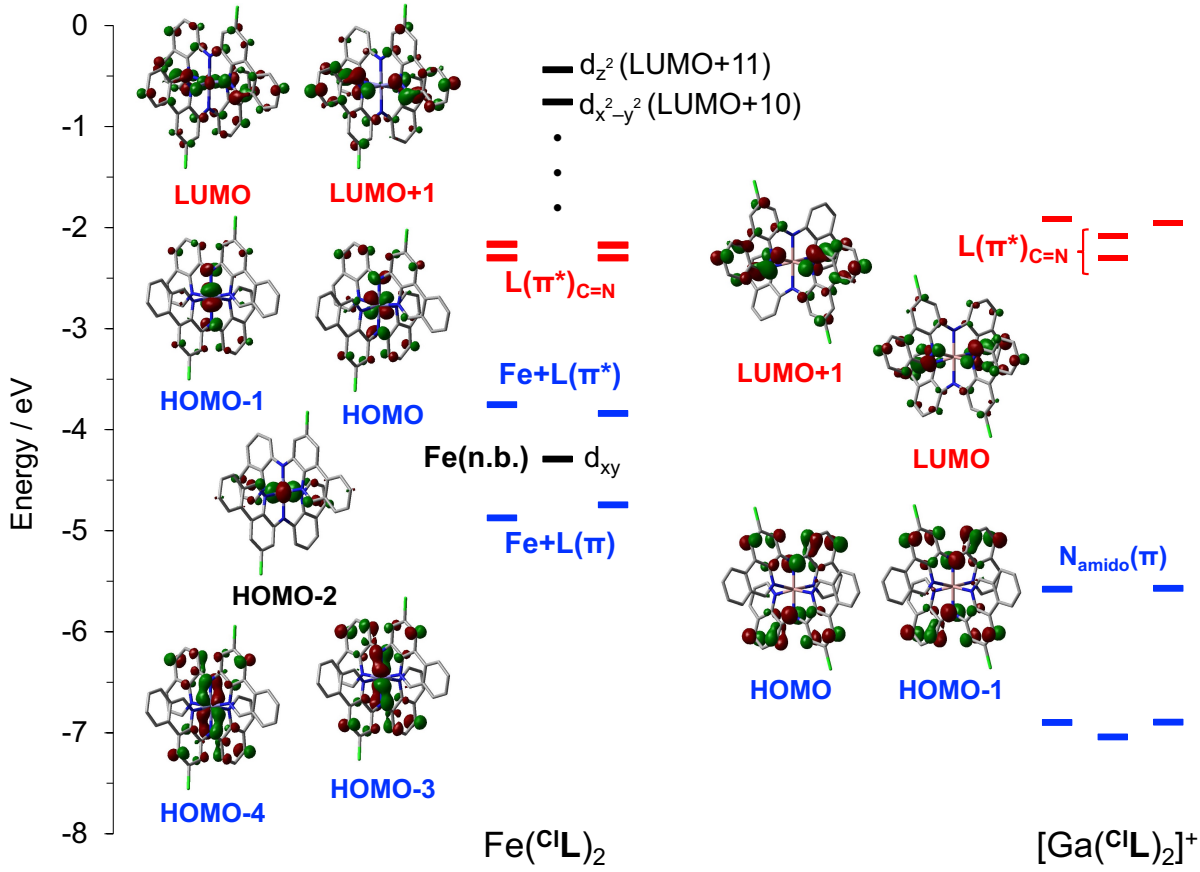

Figure 3. Selections from the ground-state MO diagrams of $Fe(^{Cl}L)_2$ and $[Ga(^{Cl}L)_2]^+$ comparing the relative energies of the metal *d*-orbitals, N_{amido} lone pairs, and ligand-based π* orbitals (highlighted in red). MOs are shown with isosurface values of 0.04 and at the SMD-M06L/6-31+G(d,p)//SMD-O3LYP/6-31+G(d,p) level of theory.

The solid-state structures of Fe(^{Cl}**L**)$_2$, [Fe(^{Cl}**L**)$_2$][PF$_6$] and [Ga(^{Cl}**L**)$_2$][PF$_6$] determined by single crystal X-ray diffraction support this orbital picture (Figure 4). In all three compounds, the metal is positioned at the center of a pseudo-octahedron comprised of two ligands with the amido nitrogen atoms *trans* to one another. The two ^{Cl}**L** ligand environments in Fe(^{Cl}**L**)$_2$ are crystallographically distinct in the solid-state, while the metal ions in [Fe(^{Cl}**L**)$_2$]$^+$ and [Ga(^{Cl}**L**)$_2$]$^+$ sit on crystallographic symmetry elements. A summary of bond distances and angles is provided in Table S6. The two Fe-N$_{phen}$ (phen = phenanthridinyl) bond distances in Fe(^{Cl}**L**)$_2$ are very similar at Fe1-N1 1.9407(13) and Fe1-N4 1.9410(13) Å, elongating slightly to 1.955(8) Å upon oxidation to [Fe(^{Cl}**L**)$_2$][PF$_6$]. The Fe-N$_{quin}$ (quin = quinolinyl) contacts are nearly identical to the Fe-N$_{phen}$ distances for Fe(^{Cl}**L**)$_2$ [Fe1-N3 1.9389(14), Fe1-N6 1.9468(14) Å] and are again not statistically altered in the cation [Fe1-N3 1.934(8) Å]. In comparison, the Fe-N$_{amido}$ bond distance contracts significantly upon oxidation from Fe1-N2 1.9294(14)/Fe1-N5 1.9330(14) in Fe(^{Cl}**L**)$_2$ to 1.886(6) Å in [Fe(^{Cl}**L**)$_2$][PF$_6$], consistent with depopulation of an orbital with Fe-amido π-anti-bonding character. This assignment is supported by ground-state DFT calculations which confirm an Fe-N$_{amido}$ bond contraction of 0.043 Å upon oxidation to [Fe(^{Cl}**L**)$_2$][PF$_6$] (Table S7), very close to the 0.045 Å observed experimentally and accompanied by an increase in the Fe-N$_{amido}$ Mayer bond order[42] ([Fe(^{Cl}**L**)$_2$]$^+$, 1.3; [Fe(^{Cl}**L**)$_2$], 1.1).

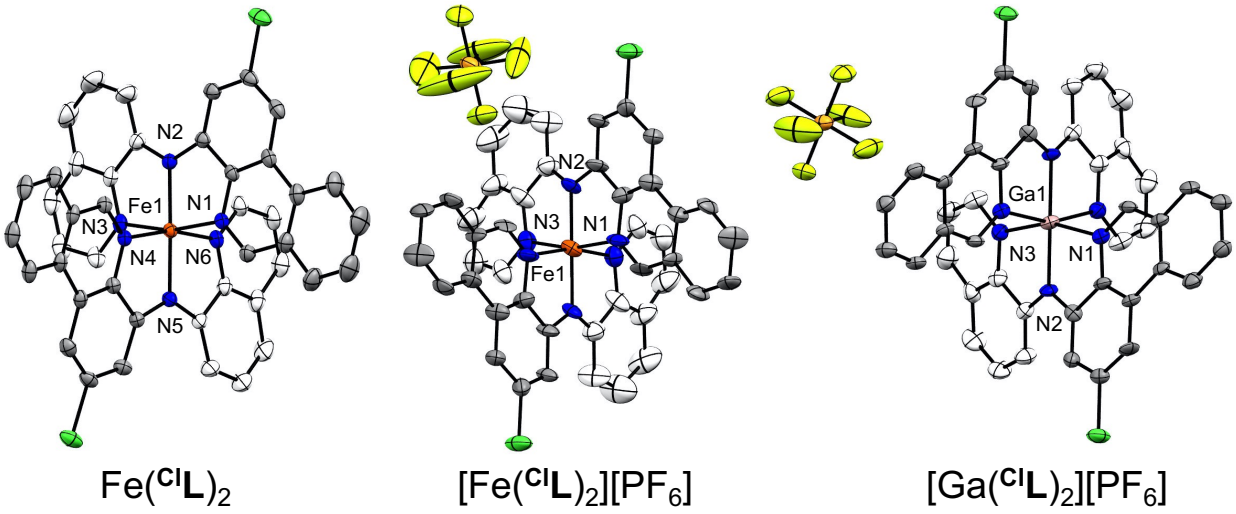

Figure 4. Solid-state structures of Fe(^{Cl}**L**)$_2$, [Fe(^{Cl}**L**)$_2$][PF$_6$] and [Ga(^{Cl}**L**)$_2$][PF$_6$] with thermal ellipsoids shown at 50% probability levels. Hydrogen atoms, co-crystallized solvent molecules and selected atom labels (including for symmetry-generated atoms) are omitted for clarity.

Optical Spectroscopy

The calculated and solid-state structures of the [Fe(^{Cl}**L**)$_2$]$^{0/+}$ redox pair thus validate the description of the frontier orbital manifold as an intermediate case of the 'HOMO inversion'[36] model, which predicts strong absorptive cross-sections across the visible range. Indeed, the electronic absorption spectrum of Fe(^{Cl}**L**)$_2$ (Figure 5) shows panchromatic absorption from the edge of the UV region, tailing off only near 900 nm, and large absorptivity values ($\varepsilon > 5000$ M^{-1} cm^{-1}) consistent with CT-type transitions. Time-dependent DFT (TD-DFT) simulations (Figure S7) revealed the lowest-energy spectral manifold (650-900 nm) is dominated by six key transitions, in which electron density is relocated from occupied Fe+L(π*) anti-bonding orbitals (HOMO, HOMO-1) to *N*-heterocycle ligand-based π*-acceptor MOs (LUMO through to LUMO+3; Table S8) and can be described as '$\pi_{\text{anti-bonding}}$-to-ligand charge-transfer' (PALCT) in character.[43] In comparison, the prominent absorption bands in the visible region of the spectrum of [Ga(^{Cl}**L**)$_2$][PF$_6$] are assigned

to electronic excitations involving the degenerate HOMO and HOMO-1 (Figure S8, Table S9), which contain significant contributions from the N_{amido} lone pairs (19%; Table S3), and the π*-orbitals of the phenanthridine arms (LUMO, LUMO+1). Thus, the low energy absorptions of [Ga(**^{Cl}L**)$_2$][PF_6] have mixed intra/inter-ligand charge-transfer (ILCT) character.

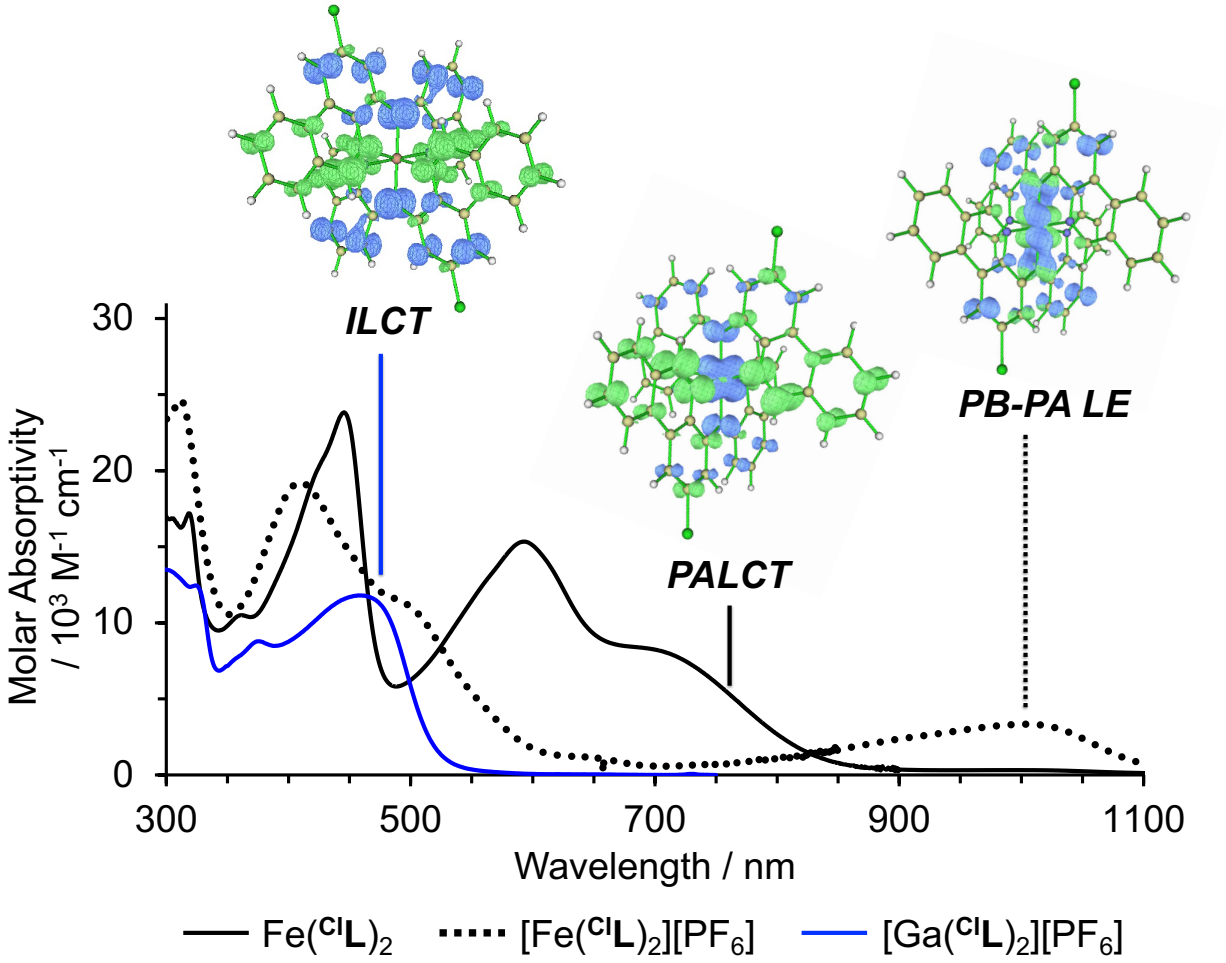

Figure 5. Steady-state UV-Vis absorption spectra of Fe(**^{Cl}L**)$_2$ (—), [Fe(**^{Cl}L**)$_2$][PF_6] (···) and [Ga(**^{Cl}L**)$_2$][PF_6] (—) in acetonitrile at 295 K and TD-DFT difference map (SMD-M06L/6-31+G(d,p)//SMD-O3LYP/6-31+G(d,p) for Fe(**^{Cl}L**)$_2$ and [Fe(**^{Cl}L**)$_2$]$^+$; SMD-PBE0/6-31+G(d,p)//SMD-O3LYP/6-31+G(d,p) for [Ga(**^{Cl}L**)$_2$]$^+$) calculated in acetonitrile showing electron density gain (green) and depletion (blue) distribution maps (isosurface = 0.002) of the transitions associated with the lowest energy absorptions of each species.

For the one-electron oxidized $[Fe(^{Cl}\mathbf{L})_2][PF_6]$, most of the absorptive cross-section between ~600-900 nm is attenuated, consistent with loss of the low energy PALCT transitions. Strong, broad CT transitions are evident at 410 and 495 nm (ε = 10-20 mM^{-1} cm^{-1}), while a low-energy absorption arises with a peak maximum at 1002 nm. This new feature falls in between that of $[Fe(^{tBu}\mathbf{L})_2][PF_6]$ (λ_{max} = 1024 nm) and $[Fe(^{CF3}\mathbf{L})_2][PF_6]$ (λ_{max} = 996 nm) and is assigned by TD-DFT (Figure S9, Table S10) to involve electron-transfer between the filled MO that retains π(d+p) Fe-N_{amido} bonding character [HOMO-2(β)] and the singly-occupied π^*(p+d) N_{amido}-Fe anti-bonding MO (here called the LUMO(β)). This transition can therefore be assigned as generating a locally excited (LE) state with $\pi_{bonding}$-to-$\pi_{anti\text{-}bonding}$ character (PB-PA LE) with limited electronic redistribution between the donor and acceptor orbitals, as reflected in the electron-hole difference map shown in Figure 5. The spectra of $[Fe(^{Cl}\mathbf{L})_2][PF_6]$ and $Fe(^{Cl}\mathbf{L})_2$ can be fully reproduced by spectroelectrochemistry (Figure S10).

Excitation into the lowest energy manifold of $Fe(^{Cl}\mathbf{L})_2$ should therefore populate low-lying excited states with PALCT character. DFT optimization of the structure of the lowest energy triplet state of $Fe(^{Cl}\mathbf{L})_2$ starting from the ground-state equilibrium geometry converged to a structure with ^{3}PALCT character (Figure S11, Table S11), with a contraction of the Fe-N_{amido} bonds by 0.041 Å nearly identical to that observed upon oxidation (Table S7); $[Fe(^{Cl}\mathbf{L})_2][PF_6]$ is therefore a structural proxy for the ^{3}PALCT excited state. In contrast, should rapid excited-state decay follow the usual pathway of Fe(II) coordination compounds and populate a metal-centered state via a ^{3}MLCT$\rightarrow$^{3}MC$\rightarrow$^{5}MC cascade,[44] all metal-ligand bonds would be expected to elongate. Modeling the nominally $^5T_{2g}$ MC state under octahedral symmetry accordingly shows a lengthening by 0.168 Å of the Fe-N_{amido} bonds and 0.247 Å (average) for the Fe-N_{quin} and Fe-N_{phen} bonds. The structure of the lowest energy ^{3}MC (e.g., $^3T_{1g}$) state similarly exhibited longer metal-ligand bonds – although

to a lesser extent due to population of a single antibonding e_g* orbital as opposed to two in the $^5T_{2g}$ state. Thus, compared to traditional Fe(II) polypyridyl complexes such as $[Fe(bpy)_3]^{2+}$ or $[Fe(terpy)_2]^{2+}$, in which the MLCT excited state exhibits very little structural distortion relative to the ground state,[45] DFT predicts far greater structural differences between CT and MC states in $Fe(^{Cl}\mathbf{L})_2$, imposing a larger inner-sphere reorganization energy cost for electron-transfer from CT to MC states.

To verify that extended excited-state lifetimes are accessible for $Fe(^{Cl}\mathbf{L})_2$, transient absorption (TA) differential pump-probe spectra were collected (see Supporting Information p. SI-38-41). Solutions were selectively excited into the low energy side of the broad CT absorption manifold ($\lambda_{excitation}$ = 780 nm) using 150 fs laser pulses and probed with broadband white light. Similar TA spectra were obtained at all time delays, with a prominent excited state absorption (ESA) feature at ~480 nm and a ground state bleach (GSB) coinciding with the CT absorption manifold. The ESA feature is faithfully reproduced by the difference spectrum calculated from spectroelectrochemically-generated absorption spectra of $[Fe(^{Cl}\mathbf{L})_2]^+$ and $[Fe(^{Cl}\mathbf{L})_2]^-$, highlighted convincingly in Figure 6a. In combination with the bleach of the ground state CT absorption manifold, the observation of this ESA feature in the TA spectra and correlation to the redox-based difference spectrum is indicative of a CT excited state.[40] All TA features evolve and decay with identical lifetimes, and the behavior is best described as instrument response function (IRF)-limited spectral evolution, followed by monoexponential decay with a ~3 ns time constant (Figure 6b; see Table S12 and SI for further discussion and figures). While the long-lived excited state is assigned to have CT character in $Fe(^{Cl}\mathbf{L})_2$ and related Fe-amido complexes due the fidelity of the transient spectra and redox-based calculated spectra, without an optical signature of the ligand

radical anion/oxidized species at longer wavelengths (> 800 nm) this assignment is incomplete and the topic of ongoing time-resolved X-ray spectroscopy studies.

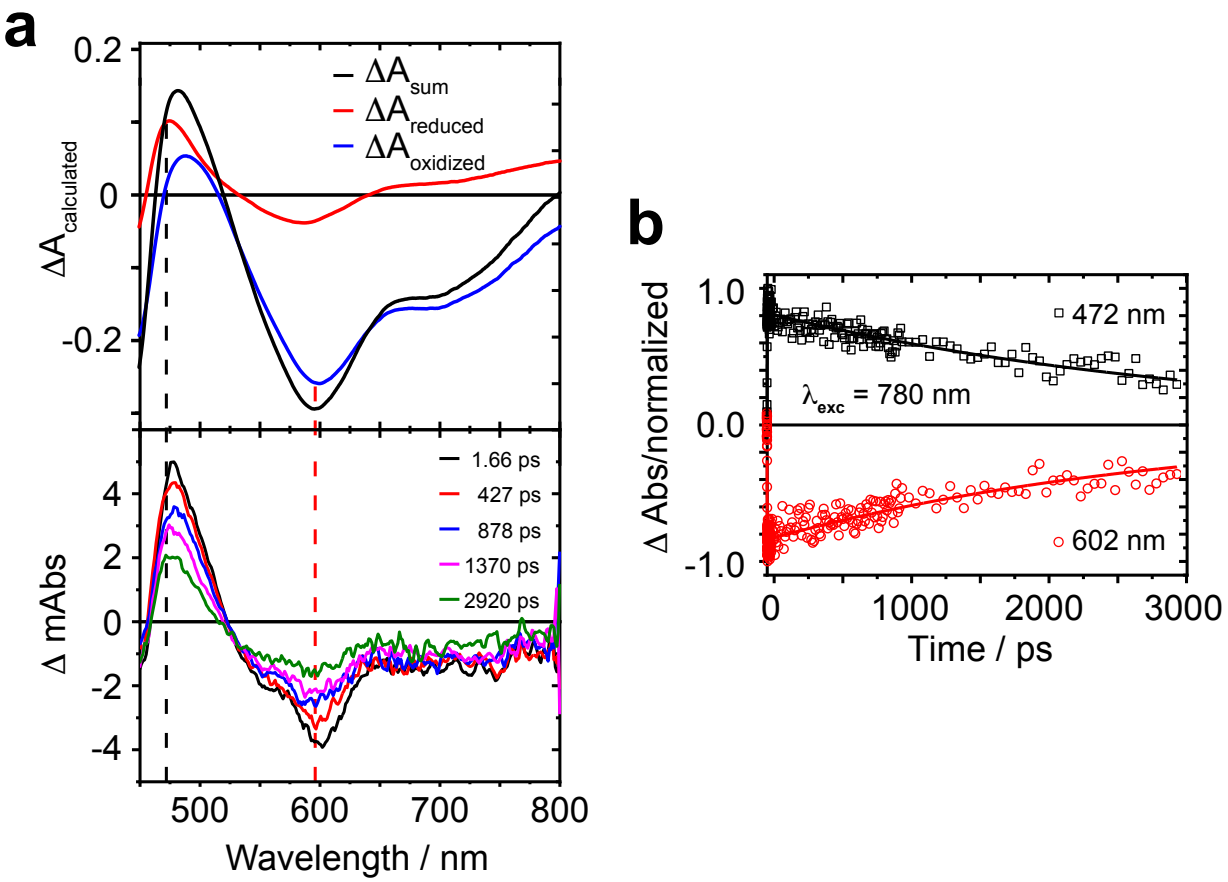

Figure 6. (a) Redox-based calculated difference spectra of $[Fe(^{Cl}L)_2]^{0/+}$ (top) and transient absorption spectra (bottom) of $Fe(^{Cl}L)_2$ in toluene at indicated time delays. The close match highlights the charge-transfer nature of the excited state. (b) Kinetic traces (see legend) and exponential fits (solid lines, fitting results are summarized in Table S12) following the decay of both the excited-state absorption and ground-state bleach at indicated wavelengths.

X-Ray Absorption Spectroscopy

Fe(^{Cl}**L**)$_2$ thus combines congruent electronic structure and photophysical properties with Fe(^{R}**L**)$_2$ (R = *t*Bu, CF_3)[37] and we therefore proceeded to investigate this compound using X-ray absorption and inelastic scattering experiments. Normalized X-ray absorption (XAS) spectra were obtained at both the Fe L_3-edge and N K-edge (Figure 7; see Figure S15 for spectra covering Fe $L_{2,3}$-edges). At the Fe L-edge, dipole-allowed Fe 2p→3d transitions are observed. Due to large spin-orbit coupling of the final state 2p core-hole (ξ_{2p}), the L-edge splits into two features, the L_3-edge (J_{2p} = 3/2) and the L_2-edge (J_{2p} = 1/2), separated by $\frac{3}{2}\xi_{2p}$ (*ca.* 12.4 eV[46]). We restrict our analysis to the more intense, lower energy L_3-edge data.

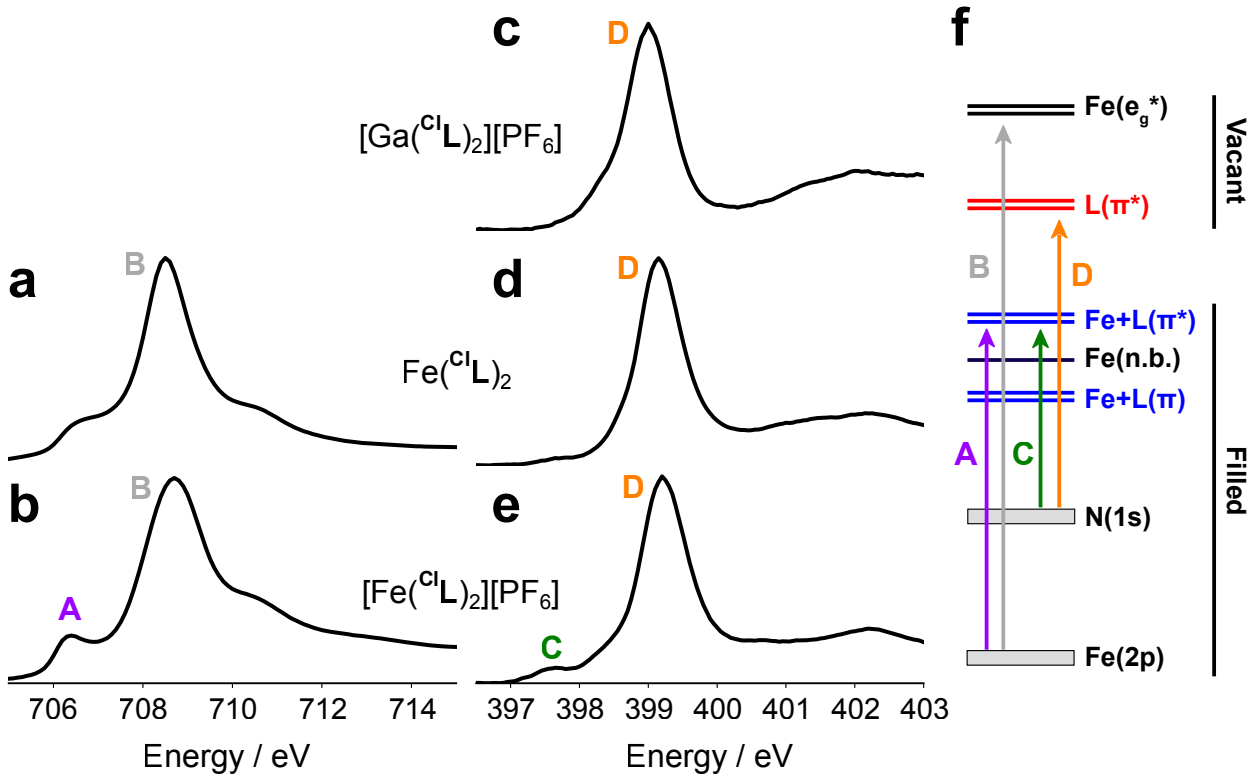

Figure 7. Normalized Fe L_3-Edge XAS spectra of (a) Fe(^{Cl}**L**)$_2$ and (b) [Fe(^{Cl}**L**)$_2$][PF_6], normalized N K-Edge XAS spectra of (c) [Ga(^{Cl}**L**)$_2$][PF_6], (d) Fe(^{Cl}**L**)$_2$ and (e) [Fe(^{Cl}**L**)$_2$]PF_6, and (f) schematic depiction of observed transitions, using [Fe(^{Cl}**L**)$_2$][PF_6] electronic configuration. Transition labels and colors correspond to labelled spectral features.

For the sake of simplicity and to assist comparison to prior studies, we will use octahedral symmetry labels for discussing and interpreting Fe L-edge XAS results. The impact of lower symmetry on the spectra and our interpretation will be subsequently addressed. For low-spin octahedral Fe(II) complexes, the t_{2g} orbital set is fully occupied. Consequently, only excitations into the e_g* orbital set can be observed. The dominant feature (**B**) in Fe L_3-edge XAS observed at 708.5 eV for Fe(^{Cl}**L**)$_2$ (Figure 7a) and [Fe(terpy)$_2$][PF$_6$]$_2$ therefore corresponds to promotion of an Fe 2p electron into the unoccupied e_g* orbital set.[33,46–50] The lower energy shoulder and higher energy satellite peaks arise due to crystal field and charge-transfer multiplet effects. Indeed, crystal field multiplet calculations using 10Dq and β parameters derived from Tanabe-Sugano analysis of Fe 2p3d RIXS spectra (see below) are sufficient to reproduce the main Fe L_3-edge XAS spectral features of both Fe(^{Cl}**L**)$_2$ and [Fe(terpy)$_2$][PF$_6$]$_2$ (Figure S16), indicating that any splitting of the nominally e_g* orbital set from descent of symmetry ($\Delta E_{LUMO+10/LUMO+11}$ = 0.32 eV from DFT) is unobservable within the spectral broadening. Although crystal field multiplet calculations reproduce the main spectral features of Fe(^{Cl}**L**)$_2$, some intensity in the lower energy shoulder is not accounted for. This intensity can be accounted for using charge-transfer multiplet (CTM) calculations including ligand-to-metal charge-transfer (LMCT) parameters to model the effect of mixing the t_{2g} orbitals with occupied ligand-based π orbitals (see Supporting Information p. SI-43-49 for further discussion). The corresponding spectrum of [Fe(^{Cl}**L**)$_2$][PF$_6$] also contains an Fe 2p→3e_g* absorption feature (**B**) at 708.7 eV (Figure 7b). The shift of this feature to higher energy relative to that of Fe(^{Cl}**L**)$_2$ is consistent with a decrease of electron density about the metal, as observed in previous work.[46,48,50] The magnitude of the shift (*ca*. 0.2 eV), however, is significantly smaller than that observed for ferrous/ferric Fe(II/III) redox-related pairs in less covalent complexes. For example, a 0.7-0.9 eV shift in the energy of feature **B** was reported for [Fe(CN)$_6$]$^{3-}$

$^{/4-}$, while a difference of 1.4 eV was observed for $[Fe(tacn)_2]^{3+/2+}$ (tacn = 1,4,7-triazacyclononane).[48,50] Comparing these latter sets of complexes, the smaller shift for $[Fe(CN)_6]^{3-/4-}$ compared to $[Fe(tacn)_2]^{3+/2+}$ was attributed to enhanced metal-ligand covalency due to π-backbonding with the cyanide ligands[48] which dampens the change in the Fe effective nuclear charge (Z_{eff}) upon oxidation/reduction. The even smaller shift of feature **B** seen for $[Fe(^{Cl}\mathbf{L})_2]^{+/0}$ therefore emphasizes the high degree of metal-ligand covalency introduced by the amido donor ligands. An additional feature (**A**) is also observed at 706.4 eV for $[Fe(^{Cl}\mathbf{L})_2][PF_6]$, which corresponds to promotion of an Fe 2p electron to the nominally Fe t_{2g} hole (denoted Fe+L(π*) in Figure 7f). Feature **A** is less clearly resolved from **B** than for previously reported Fe(III) complexes, presumably as a consequence of Fe t_{2g} and N_{amido} 2p mixing. Although coincidentally appearing at similar energy to the low energy shoulder of **B** in the Fe(III) complexes, the shoulder of the Fe(II) complexes is not assigned as **A** as it arises from the CT character of the t_{2g} orbitals as described above and in the Supporting Information, as opposed to excitation into a nominally t_{2g} hole for the Fe(III) complex.

Unlike for $Fe(^{Cl}\mathbf{L})_2$, crystal field multiplet calculations using only 10Dq and β parameters derived from Tanabe-Sugano analysis of Fe 2p3d RIXS spectra are insufficient to model the Fe L_3-edge XAS spectrum of $[Fe(^{Cl}\mathbf{L})_2][PF_6]$. It has been previously demonstrated that CTM calculations including both crystal field and CT parameters are needed to accurately describe Fe L-edge XAS spectra of Fe(III) complexes.[48,49,51] Mixing of ligand-to-metal charge-transfer (LMCT) character into the ground state electronic structure models the effect of ligand π-donation not accounted for by the crystal field description and qualitatively reproduces the key spectral features of the $[Fe(^{Cl}\mathbf{L})_2][PF_6]$ Fe L-edge XAS spectrum (Figure S16; additional discussion on CTM calculations is presented in Supporting Information p. SI-43-49). The observed spectrum of

[Fe(^{Cl}**L**)$_2$][PF$_6$] is therefore consistent with a low-spin Fe(III)-type system, as concluded from Fe 2p3d RIXS, magnetic moment measurement, X-ray crystallography and DFT calculations, as well as EPR and Mössbauer spectroscopy of related complexes.[37]

At the N K-edge, dipole-allowed N 1s→2p transitions are observed. As discussed above, [Ga(^{Cl}**L**)$_2$][PF$_6$] represents the ligand spectrum in the absence of metal-ligand orbital mixing.[38] The main N K-edge XAS feature observed for [Ga(^{Cl}**L**)$_2$][PF$_6$] at 399.0 eV (Figure 7c, **D**) is therefore assigned to ligand-localized transitions. TD-DFT calculations support this assignment (Figure S20, Table S13), predicting contributions of three transitions from quinolinyl and phenanthridinyl N 1s to the unoccupied ligand-localized frontier molecular orbitals (LUMO through LUMO+3), with the weak low-energy shoulder arising from a single transition from N_{amido} 1s to these same unoccupied ligand-localized MOs. This ligand-centered feature (**D**) is conserved across the series of complexes (Figure 7c-e). The spectrum of [Fe(^{Cl}**L**)$_2$][PF$_6$] exhibits an additional weak feature at ca. 397.6 eV (**C**). TD-DFT calculations predict this feature to arise from transitions from the two N_{amido} 1s orbitals to the Fe+L(π*) orbital. XAS is an element-specific technique; at the N K-edge acceptor orbitals must necessarily possess N 2p character to be observed. The observation of this feature (**C**) therefore provides direct experimental evidence of Fe(t_{2g})-N_{amido}(2p) mixing and validates the electronic structure predicted from first principles and by DFT calculations.

N K-Edge (1s2p) Resonant Inelastic X-Ray Scattering

N 1s2p RIXS at the N K-edge (Figure 8) provides further evidence for strong metal-ligand covalency in Fe(^{Cl}**L**)$_2$ and [Fe(^{Cl}**L**)$_2$][PF$_6$] (see also Figures S21 and S23, respectively; Figure S24 contains spectra of [Ga(^{Cl}**L**)$_2$][PF$_6$]). Also known as X-ray resonance Raman spectroscopy, the

operating principle of RIXS is that when the incident X-ray energy (E_i) coincides with an electronic transition, photons inelastically scatter off the resonant core excited state (with energy E_s), forming a valence excited state, as illustrated schematically in Figures 8e and 9c. The energy-transfer spectrum (E_i-E_s) directly measures the energy of the valence excited states associated with a specific X-ray resonance. The Raman selection rules and atomic specificity of RIXS dictate that the occupied orbital involved in the scattering process necessarily possesses the same character as the unoccupied orbital in the underlying electronic transition (*i.e.*, N 2p for N 1s2p RIXS) and that the final valence excited state must conserve parity. It should therefore be noted that electronic UV-Visible absorption spectroscopy and RIXS do not necessarily probe the same valence excited states.

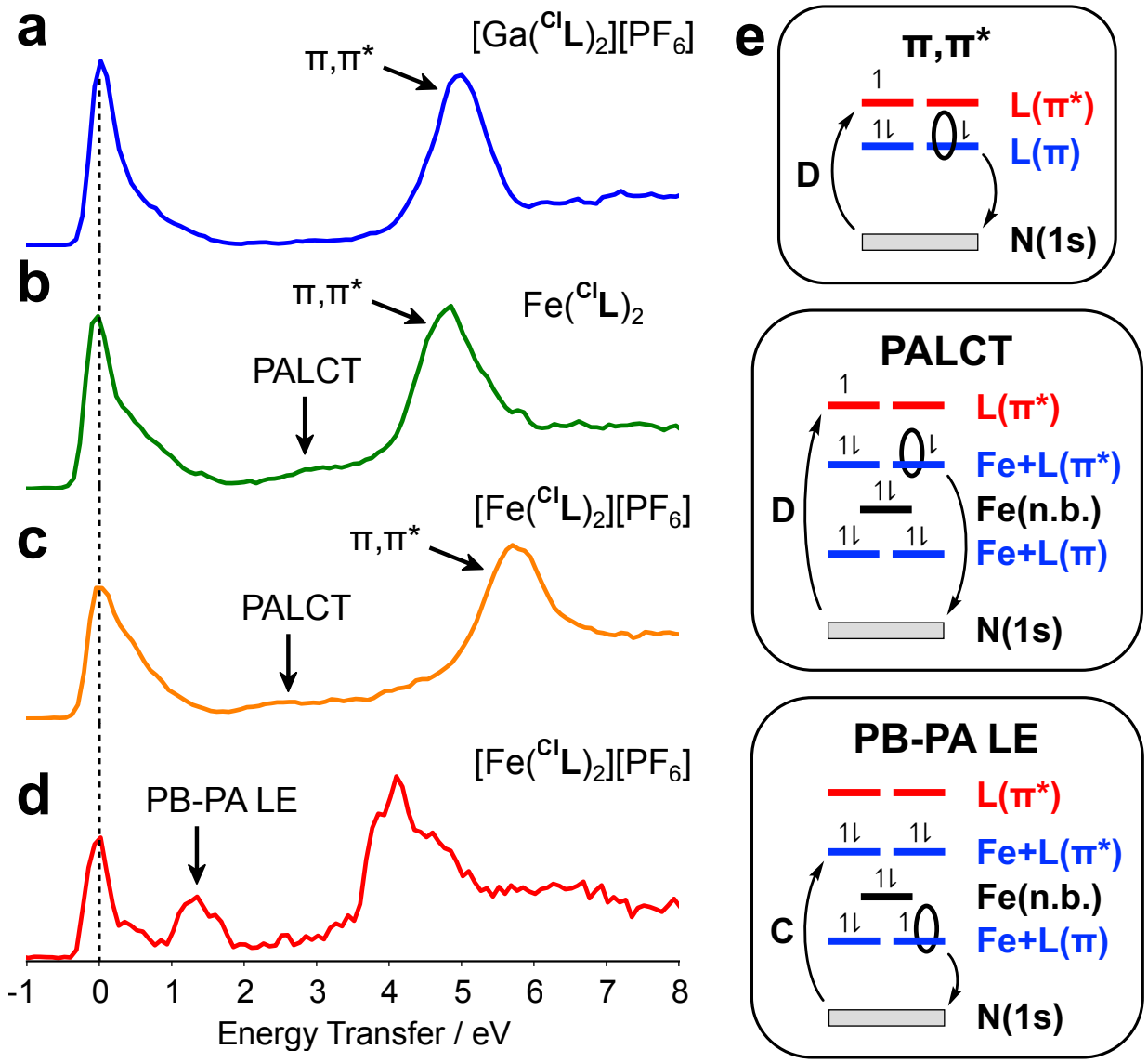

Figure 8. N 1s2p RIXS spectra obtained upon excitation into the main resonance (band "**D**" in Fig. 7c-e) for (a) $[Ga(^{Cl}L)_2][PF_6]$ (E_i = 399.3 eV), (b) $Fe(^{Cl}L)_2$ (E_i = 399.4 eV) and (c) $[Fe(^{Cl}L)_2][PF_6]$ (E_i = 399.3 eV), and (d) into the weaker 1s→M+L(π*) resonance (band "**C**" in Fig. 7e) for $[Fe(^{Cl}L)_2][PF_6]$ (E_i = 397.6 eV) at the N K-edge. Dotted black vertical line corresponds to the elastic scattering peak at 0 eV. The high energy-transfer shoulder of the elastic scattering peak arises from vibrational resonance Raman scattering; (e) Schematic depiction of N 1s2p RIXS assignments. Depicted electronic configurations correspond to named final states, circles depict holes.

Given the absence of metal-ligand orbital mixing in $[Ga(^{Cl}\mathbf{L})_2][PF_6]$,[38] all final states observed in N 1s2p RIXS necessarily arise from ligand-centered π,π* transitions. Spectral differences between $Fe(^{Cl}\mathbf{L})_2$ and $[Ga(^{Cl}\mathbf{L})_2][PF_6]$ are therefore diagnostic of transitions involving valence orbitals with mixed metal-ligand character. For $[Ga(^{Cl}\mathbf{L})_2][PF_6]$, following excitation into the high-energy side of the dominant N K-edge XAS feature at 399.3 eV (**D**, Figure 7c), only a single π,π* final state is observed at 5.0 eV (Figure 8a). For $Fe(^{Cl}\mathbf{L})_2$, following excitation into the same dominant N K-edge XAS feature at 399.4 eV (**D**, Figure 7d), a similar π,π* final state is observed at 4.8 eV as well as an additional low energy feature at 3.0 eV not present in the $[Ga(^{Cl}\mathbf{L})_2][PF_6]$ spectrum (Figure 8b). This additional feature corresponds to scattering off the Fe+L(π*) orbitals and is therefore assigned as a ^{1}PALCT final state. The ability to access this state with N 1s RIXS demonstrates the mixed metal-ligand character of the hole in the PALCT final state. Similar N 1s2p RIXS features (assigned in the literature as MLCT) have been previously observed for Fe(II) cyanide complexes (in which the cyanide N 2p orbitals strongly mix with the Fe $3t_{2g}$ orbitals),[47,50] but not for $[Fe(bpy)_3]^{2+}$ (in which the N 2p and Fe $3t_{2g}$ orbitals do not substantively mix).[47]

Upon excitation into the dominant N K-edge XAS feature of $[Fe(^{Cl}\mathbf{L})_2][PF_6]$ at 399.3 eV (**D**, Figure 7e), a π,π* final state is observed at 5.7 eV (Figure 8c). The shift of this feature to higher energy relative to that of $Fe(^{Cl}\mathbf{L})_2$ is presumably a consequence of oxidation being partially ligand-based, thanks to the mixed Fe-N_{amido} character of the HOMO. Low energy PALCT scattering is also observed between 2-4 eV. Upon excitation into the weak N 1s→Fe+L(π*) transition at 397.6 eV (**C**, Figure 7e), a ligand-to-$\pi_{anti\text{-}bonding}$ charge-transfer (LPACT) feature (corresponding to resonant scattering off deep ligand-localized orbitals) is observed at 4.1 eV, as well as an additional feature at 1.3 eV (Figure 8d) corresponding to a ^{2}PB-PA LE final state. The energy of this feature

is in good agreement with the difference in energy between the Fe+L(π) and Fe+L(π*) orbitals estimated by DFT calculations, as well as the energy of the optical ^{2}PB-PA LE absorption (Figure 5). Observation of these PALCT and PB-PA LE features in N 1s2p RIXS spectra provides direct experimental evidence for substantial mixing of Fe t_{2g} and ligand N_{amido} 2p orbitals.

Fe L-Edge (2p3d) Resonant Inelastic X-Ray Scattering

Fe 2p3d RIXS spectra obtained for Fe(^{Cl}**L**)$_2$ and [Fe(terpy)$_2$](PF$_6$)$_2$ upon excitation into the e_g* resonance at the Fe L_3-edge are presented in Figure 9a-b (see also Figures S21-S22; Figure S23 contains spectra of [Fe(^{Cl}**L**)$_2$][PF$_6$]). In Fe 2p3d RIXS, the incident X-ray energy is resonant with 2p$\rightarrow$3d transitions. As with the Fe L-edge XAS results, we will use octahedral symmetry labels for discussing and interpreting Fe L-edge RIXS results and subsequently address the impact of lower symmetry on the collected spectra and our interpretation. When tuned to the e_g* resonance, the Raman selection rules dictate that the dominant features observed will correspond to MC final states arising from nominally $t_{2g}\rightarrow e_g$* transitions (Figure 9c). For low-spin octahedral Fe(II) complexes with d^6 electronic configurations, the ground-state is $^1A_{1g}$ and MC states arising from single electron excitations have $^1T_{1g}$, $^3T_{1g}$, $^1T_{2g}$ and $^3T_{2g}$ symmetry. It is important to note that spectral features arising from these MC states in the RIXS spectrum do not correspond to vibrationally relaxed energy minima but rather to excitation energies associated with the ground-state geometry (i.e., vertical energies on a potential energy surface diagram, consistent with the Franck-Condon principle).

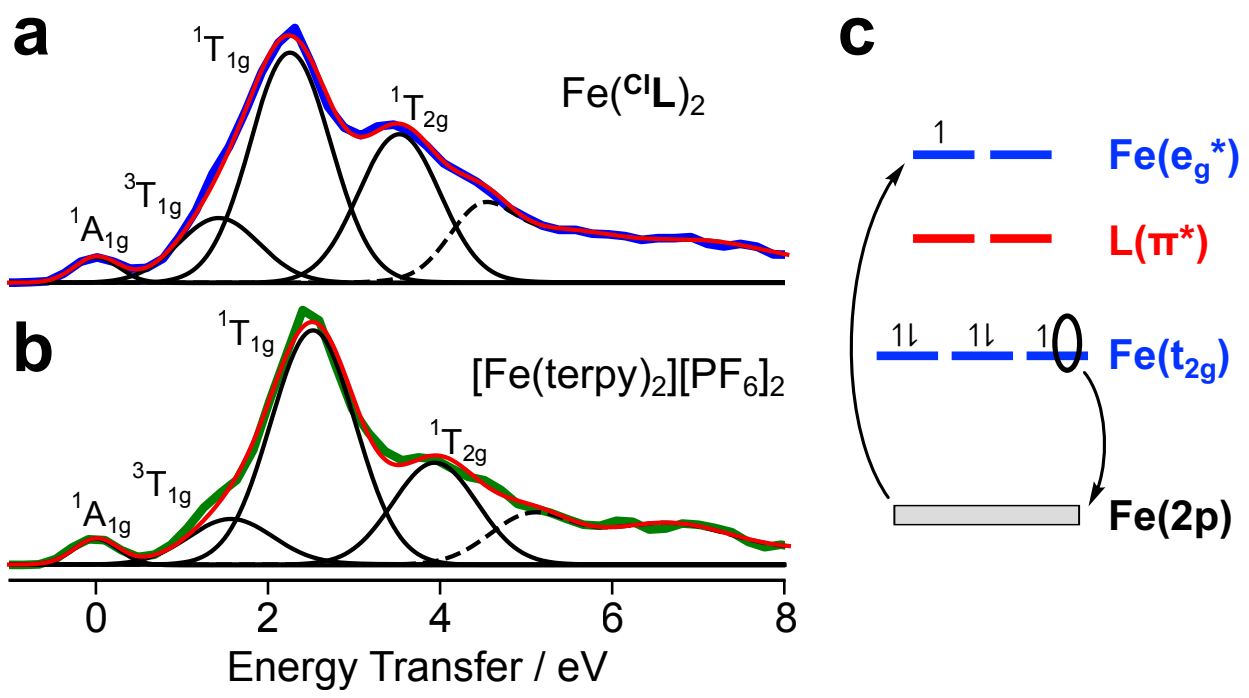

Figure 9. Fe 2p3d RIXS spectra obtained upon excitation into the e_g* resonance at the Fe L_3-edge for (a) Fe(^{Cl}**L**)$_2$ (solid blue trace, E_i = 708.5 eV) and (b) [Fe(terpy)$_2$][PF$_6$]$_2$ (solid green trace, E_i = 708.7 eV) and the corresponding Tanabe-Sugano fits (red traces). Black traces correspond to individual contributions from MC (solid) states and the high energy tail (dashed) to the fit; (c) Schematic depiction of Fe 2p3d RIXS processes that result in MC final states for an octahedral d^6 Fe(II) complex. Depicted electronic configuration corresponds to final state, circles depict holes.

In Figure 9, the weak feature at 0 eV corresponds to inelastic scattering where the electronic final state remains $^1A_{1g}$ (the ground state) but unresolved vibrational excitations contribute to the RIXS intensity. The main features (1-5 eV) correspond to the aforementioned single electron (t_{2g}→e_g*) excitation terms, and the high energy tail (> 5 eV) is assigned to states arising from scattering off deeper ligand-based orbitals with appropriate symmetry. It should be noted that multi-electron excitation terms can also contribute to the scattering intensity in this region due to mixing with single excitation terms.[33]

As discussed above, Fe L-edge XAS spectra are satisfactorily modelled under the assumption of octahedral symmetry, with no observable splitting of the Fe e_g orbital set. However, N 1s2p RIXS convincingly indicates splitting of the Fe t_{2g} orbital set due to mixing with N_{amido} 2p orbitals. Despite this, the Fe 2p3d RIXS spectral profile obtained upon excitation into the e_g* resonance at the Fe L_3-edge for Fe(^{Cl}**L**)$_2$ is qualitatively very similar to that of $[Fe(terpy)_2]^{2+}$ and previously reported Fe complexes for which the approximation of octahedral symmetry was found to be valid,[32,48] exhibiting no additional fine structure that can be attributed to splitting of the octahedral terms. We therefore find the approximation of octahedral symmetry to be valid for the Fe L-edge spectroscopy, with splitting of terms due to splitting of the Fe t_{2g} orbital set unobservable within the resolution of the RIXS experiment.

Spectral fitting using Tanabe-Sugano parameters yields the red fits in Figure 9 (see Figures S25-S28 and Supporting Information p. SI-57-64 for full discussion). Consistent with previous work,[52] the most intense feature is assigned to the $^1T_{1g}$ MC state, the low energy shoulder to the $^3T_{1g}$ state, and the higher energy feature to the $^1T_{2g}$ state. The $^3T_{2g}$ state occurs at very similar energies to the $^1T_{1g}$ state and cannot be deconvolved in our fit. In our Tanabe-Sugano fitting procedure, term energies are derived from only two free fit parameters: the octahedral splitting energy, 10Dq, and the nephelauxetic scaling parameter, β, which scales the free-ion Racah parameters (which describe electron-electron repulsion in the d orbitals) obtained from atomic Hartree-Fock calculations (Tables S14-S15). These parameters and the derived term energies are presented in Table 1. As can be seen in Table 1, the nephelauxetic reduction in the electron-electron repulsion energy for Fe(^{Cl}**L**)$_2$ compared to $[Fe(terpy)_2]^{2+}$, due to the increased covalency of Fe(^{Cl}**L**)$_2$, counteracts the impact of the smaller 10Dq for Fe(^{Cl}**L**)$_2$.

Table 1. Parameters and MC state energies (at ground-state geometry) derived from Tanabe-Sugano analysis of Fe 2p3d RIXS spectra for Fe(^{Cl}**L**)$_2$ and [Fe(terpy)$_2$][PF$_6$]$_2$.

Complex	Fe(^{Cl}**L**)$_2$	[Fe(terpy)$_2$][PF$_6$]$_2$
10Dq / eV	2.49	2.77
β	0.70	0.80
$B_{complex}$ / eV	0.10	0.12
$C_{complex}$ / eV	0.38	0.43
$^1T_{1g}$ / eV	2.25	2.51
$^1T_{2g}$ / eV	3.51	3.93
$^3T_{1g}$ / eV	1.42	1.56
$^3T_{2g}$ / eV	2.04	2.27
$^5T_{2g}$ / eV	1.64	1.77
^{3}CT / eV	1.21 [a]	1.98 [b]

[a] ^{3}PALCT; Obtained from spectral fitting of UV-Vis spectrum (Figure S29)

[b] ^{3}MLCT; from reference[53]

The spectrochemical series suggests that as a π-donor ligand, ^{Cl}**L** is a weaker-field ligand than terpy and should therefore exert a smaller 10Dq. This is indeed the case: 10Dq for Fe(^{Cl}**L**)$_2$ is 280 meV smaller than for [Fe(terpy)$_2$][PF$_6$]$_2$. The use of weak-field π-donor ligands is not a common strategy for Fe complex photosensitizer design, as it is often presumed that weakening the ligand-field leads to a leftward shift on the Tanabe-Sugano diagram (equivalent to shifting the red line in Figure 1 back to the left) and consequently lowers the energy of MC states. However, this does not account for the increase in metal-ligand covalency associated with π-donor ligands, which lowers the Racah parameter B, counterbalancing the effect of lowering 10Dq. Indeed, the increased covalency of Fe(^{Cl}**L**)$_2$ results in smaller values of B compared to [Fe(terpy)$_2$][PF$_6$]$_2$, effectively counteracting the decrease in 10Dq, such that Fe(^{Cl}**L**)$_2$ (10Dq/B = 24) actually lies slightly to the right of [Fe(terpy)$_2$][PF$_6$]$_2$ (10Dq/B = 23) on the Tanabe-Sugano diagram (see Figure S26). As a consequence, despite lowering 10Dq by 280 meV from [Fe(terpy)$_2$][PF$_6$]$_2$ to Fe(^{Cl}**L**)$_2$,

the nominally $^3T_{1g}$ and $^5T_{2g}$ MC states (which are the most relevant for excited-state deactivation) only decrease in energy by 140 and 130 meV, respectively. While not insignificant, such a decrease is substantially smaller than the anticipated 280 and 560 meV decrease corresponding to the change in 10Dq alone. This highlights the overlooked importance of metal-ligand covalency in tuning MC state energies with π-donor ligands.

From band shape analysis of its electronic absorption spectrum (Figure S29), a ^{3}PALCT energy of 1.26 eV is obtained for Fe(^{Cl}**L**)$_2$, significantly lower than for the ^{3}MLCT state of [Fe(terpy)$_2$][PF$_6$]$_2$ (1.98 eV) and strikingly close to the value determined by DFT (see Tables S11 and S16). This results in an inversion in the excited-state ordering at the ground-state geometry, whereby the lowest energy triplet state is the $^3T_{1g}$ MC state for [Fe(terpy)$_2$][PF$_6$]$_2$, but the ^{3}PALCT state for Fe(^{Cl}**L**)$_2$. In the schematic potential energy surface diagram in Figure 10, this effect is represented as a stabilization of the ^{3}CT potential energy surface relative to the MC states upon going from [Fe(terpy)$_2$][PF$_6$]$_2$ (dashed blue line) to Fe(^{Cl}**L**)$_2$ (solid blue line), decreasing the driving force for electron-transfer ($-\Delta G^0$) from the ^{3}CT to the $^3T_{1g}$ state.

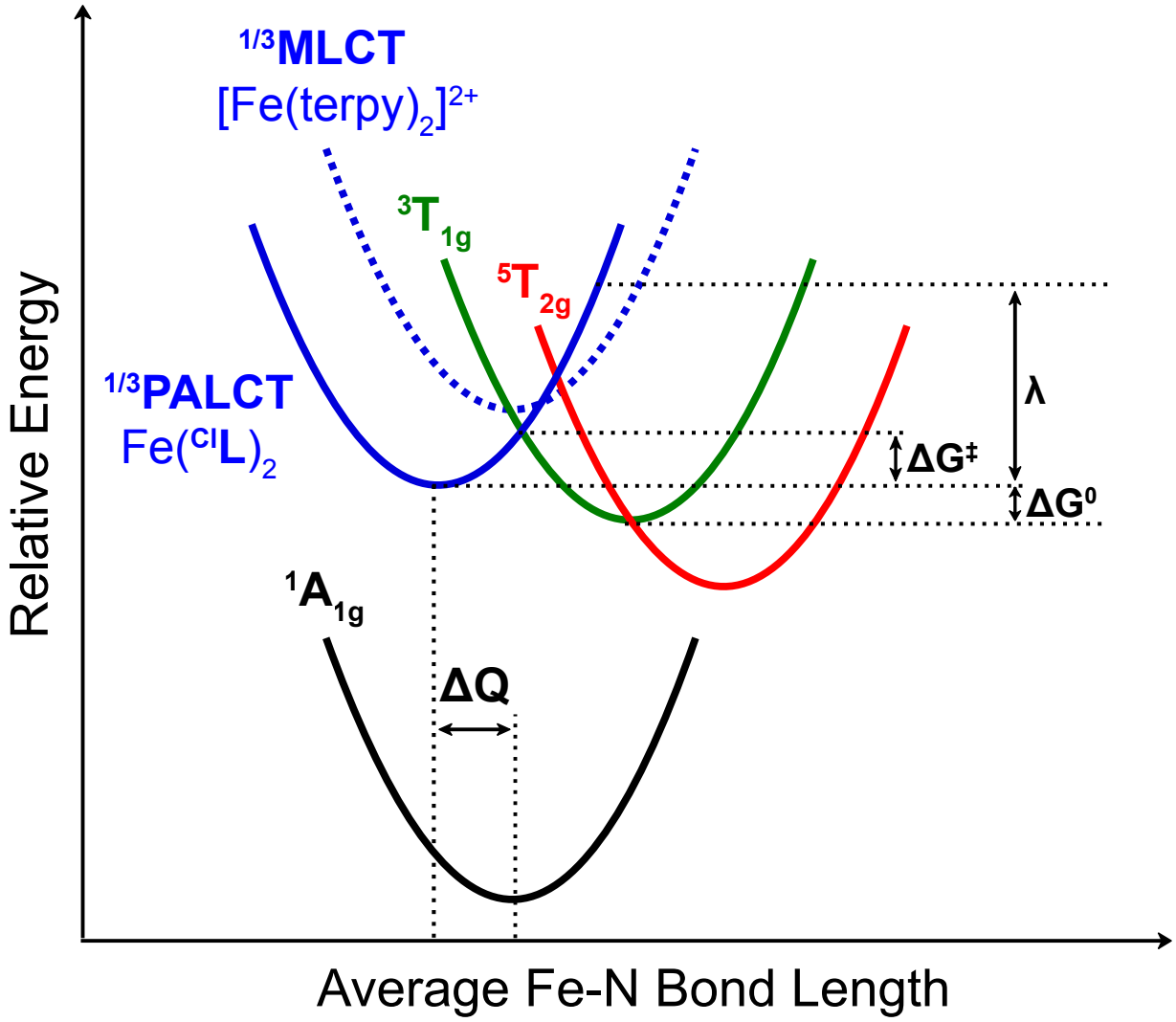

Figure 10. Schematic potential energy diagram depicting how the increased covalency of $Fe(^{Cl}L)_2$, compared to $[Fe(terpy)_2]^{2+}$, influences the vertical electronic excitation energy and the intramolecular reorganization energy associated with Fe-N bond contraction for the $[Fe(terpy)_2]^{2+}$ MLCT state (depicted with dotted blue line) and the $Fe(^{Cl}L)_2$ PALCT state (depicted with solid blue line). Vertical arrows depict relevant parameters for electron-transfer from the solid blue to solid green potential energy wells. Horizontal arrow depicts Fe-N bond contraction (ΔQ) in the MLCT excited state relative to the ground ($^1A_{1g}$) state.

Furthermore, as discussed above, unlike $[Fe(terpy)_2][PF_6]_2$, $Fe(^{Cl}L)_2$ should exhibit a metal-ligand bond *contraction* in the CT state relative to the ground-state (ΔQ, Figure 10) thanks to the Fe-N_{amido} π anti-bonding nature of the HOMO, imposing a greater inner-sphere

reorganization energy (λ) cost for electron-transfer from the ^{3}CT to the $^3T_{1g}$ MC excited state. Previous works have established that electron-transfer from the ^{3}MLCT to the $^3T_{1g}$ MC excited state is effectively barrierless ($-\Delta G^0 = \lambda$) for $[Fe(terpy)_2]^{2+}$ and related complexes.[23,44,55] Similarly, replacement of a 1,10-phenanthroline ligand in $[Fe(phen)_3]^{2+}$ with a bidentate carbene ligand was demonstrated to destabilize the $^5T_2$ ligand-field excited state, leading the charge-transfer manifold to become the dominant contributor to the excited-state spectroscopy of the molecule, and extending the CT excited state lifetime from 180 fs to 7.4 ps.[56] Here, the cumulative effect of increasing both ΔG^0 (decreasing driving force) and λ provide a mechanism for increasing the activation barrier ($\Delta G^{\ddagger}$) for electron-transfer from the ^{3}CT to $^3T_{1g}$ MC excited state.

CONCLUSIONS

In the search for molecular design principles to access long-lived CT excited states in Fe(II) complexes, efforts have predominantly focused on increasing ligand field strength to destabilize deactivating MC states. However, this approach has failed to reach nanosecond CT lifetimes, prompting the search for fundamentally new approaches. Fe(II) complexes bearing weak-field amido π-donors in the form of benzannulated, pincer-type diarylamido ligands, $Fe(^{R}\mathbf{L})_2$, present both nanosecond excited state lifetimes assigned to CT states and panchromatic absorption. As this result is contrary to expectations based on common molecular design strategies for Fe(II) photosensitizers, we sought to understand the photophysical origin of this proposed counter-intuitive behavior via XAS and RIXS at the Fe L-edge and N K-edge. Using $Fe(^{Cl}\mathbf{L})_2$, we have experimentally validated strong Fe-N_{amido} orbital mixing, demonstrating a hitherto unreported competition between decreasing 10Dq (due to the weaker ligand field exerted by π-donor ligands) and decreasing electron-electron repulsion in the Fe 3d orbitals (due to strong metal-ligand

covalency) that results in minimal stabilization of deactivating MC states in Fe($^{\mathbf{R}}$**L**)$_2$ complexes relative to more traditional Fe(II) complexes bearing polypyridyl ligands such as $[Fe(bpy)_3]^{2+}$ and $[Fe(terpy)_2]^{2+}$. While decreasing ligand field strength through the use of weak field ligands is commonly thought to simply induce a leftwards shift on a Tanabe-Sugano diagram, here, despite a lower 10Dq, Fe($^{\mathbf{Cl}}$**L**)$_2$ actually sits to the right of $[Fe(terpy)_2]^{2+}$ on a Tanabe-Sugano diagram. Moreover, as a consequence of Fe-N_{amido} orbital mixing in Fe($^{\mathbf{Cl}}$**L**)$_2$, the lowest energy ^{3}PALCT is highly stabilized relative to the ^{3}MLCT states of $[Fe(bpy)_3]^{2+}$ and $[Fe(terpy)_2]^{2+}$.

Furthermore, due to the Fe-N_{amido} anti-bonding character of the HOMO, formation of the ^{3}PALCT state should cause a metal-ligand bond contraction relative to the ground state (in contrast to the bond elongation exhibited in MC states), imbuing an inner-sphere reorganization energy cost to access the latter from the former. These three effects - stabilization of PALCT state, minimal stabilization of MC states, and inner-sphere reorganization energy cost - cumulatively provide a mechanism for increasing the activation barrier for electron-transfer from the CT to MC state manifolds. Our results highlight the importance of considering metal-ligand covalency when developing design principles to access long-lived CT excited states and provide a path towards developing Fe(II) complexes with further enhanced photophysical properties.

ASSOCIATED CONTENT

Supporting Information. Tables of bond distances and angles; tabulated redox and electronic absorption parameters; computational methodology, data tables, figures and coordinates; multi-nuclear NMR and HR-MS spectra; additional XAS and RIXS figures, tables and discussion; crystallographic information files containing all X-ray data. CCDC 2078667-2078669 contain the supplementary crystallographic data for this paper. The data can be obtained free of charge from The Cambridge Crystallographic Data Center via www.ccdc.cam.ac.uk/structures.

The following files are available free of charge:

Supporting Information File (PDF)

Crystallographic Information Files (CIF)

AUTHOR INFORMATION

Corresponding Authors

Amy A. Cordones (acordon@slac.stanford.edu)

Kelly J. Gaffney (kgaffney@slac.stanford.edu)

David E. Herbert (david.herbert@umanitoba.ca)

ORCIDs

Christopher B. Larsen: 0000-0003-3006-2408

Jason D. Braun: 0000-0002-5850-8048

Issiah B. Lozada: 0000-0002-1689-2918

Kristjan Kunnus: 0000-0002-9777-2685

Elisa Biasin: 0000-0002-7276-4224

Charles Kolodziej: 0000-0002-2921-9570

Clemens Burda: 0000-0002-7342-2840

Amy A. Cordones: 0000-0001-9897-5380

Kelly J. Gaffney: 0000-0002-0525-6465

David E. Herbert: 0000-0001-8190-2468

Author Contributions

All authors have given approval to the final version of the manuscript.

Conflicts of Interest

There are no conflicts of interest to declare.

ACKNOWLEDGMENTS

We gratefully acknowledge the Natural Sciences Engineering Research Council of Canada (DH; RGPIN-2014-03733); the Canadian Foundation for Innovation and Research Manitoba for an award in support of an X-ray diffractometer (CFI #32146); Compute Canada for access to computational resources; and CWRU for support for the Center for Chemical Dynamics. Ibrahim Alfurayj is thanked for assistance with confirmation of analysis of TA data. CL, KK, EB, AC, and KG acknowledge support from the U.S. Department of Energy, Office of Science, Basic Energy Sciences, Chemical Sciences, Geosciences, and Biosciences Division under award number DE-AC02-76SF00515. This research used resources of the Advanced Light Source, a U.S. DOE Office of Science User Facility under contract no. DE-AC02-05CH11231.

REFERENCES

(1) Arias-Rotondo, D. M.; McCusker, J. K. The Photophysics of Photoredox Catalysis: A Roadmap for Catalyst Design. *Chem. Soc. Rev.* **2016**, *45*, 5803–5820.

(2) Hagfeldt, A.; Boschloo, G.; Sun, L.; Kloo, L.; Pettersson, H. Dye-Sensitized Solar Cells. *Chem. Rev.* **2010**, *110*, 6595–6663.

(3) Narayanam, J. M. R.; Stephenson, C. R. J. Visible Light Photoredox Catalysis: Applications in Organic Synthesis. *Chem. Soc. Rev.* **2011**, *40*, 102–113.

(4) Nazeeruddin, M. K.; Pechy, P.; Renouard, T.; Zakeeruddin, S. M.; Humphry-Baker, R.; Comte, P.; Liska, P.; Cevey, L.; Costa, E.; Shklover, V.; Spiccia, L.; Deacon, G. B.; Bignozzi, C. A.; Graetzel, M. Engineering of Efficient Panchromatic Sensitizers for Nanocrystalline TiO2-Based Solar Cells. *J. Am. Chem. Soc.* **2001**, *123*, 1613–1624.

(5) Ponseca, C. S.; Chábera, P.; Uhlig, J.; Persson, P.; Sundström, V. Ultrafast Electron Dynamics in Solar Energy Conversion. *Chem. Rev.* **2017**, *117*, 10940–11024.

(6) Yoon, T. P.; Ischay, M. A.; Du, J. Visible Light Photocatalysis as a Greener Approach to Photochemical Synthesis. *Nat. Chem.* **2010**, *2*, 527.

(7) Wenger, O. S. Photoactive Complexes with Earth-Abundant Metals. *J. Am. Chem. Soc.* **2018**, *140*, 13522–13533.

(8) Förster, C.; Heinze, K. Photophysics and Photochemistry with Earth-Abundant Metals – Fundamentals and Concepts. *Chem. Soc. Rev.* **2020**, *49*, 1057–1070.

(9) Housecroft, C. E.; Constable, E. C. The Emergence of Copper(I)-Based Dye Sensitized Solar Cells. *Chem. Soc. Rev.* **2015**, *44*, 8386–8398.

(10) Magni, M.; Biagini, P.; Colombo, A.; Dragonetti, C.; Roberto, D.; Valore, Adriana. Versatile Copper Complexes as a Convenient Springboard for Both Dyes and Redox Mediators in Dye Sensitized Solar Cells. *Coord. Chem. Rev.* **2016**, *322*, 69–93.

(11) Zhang, Y.; Petersen, J. L.; Milsmann, C. A Luminescent Zirconium(IV) Complex as a Molecular Photosensitizer for Visible Light Photoredox Catalysis. *J. Am. Chem. Soc.* **2016**, *138*, 13115–13118.

(12) Zhang, Y.; Lee, T. S.; Favale, J. M.; Leary, D. C.; Petersen, J. L.; Scholes, G. D.; Castellano, F. N.; Milsmann, C. Delayed Fluorescence from a Zirconium(IV) Photosensitizer with Ligand-to-Metal Charge-Transfer Excited States. *Nat. Chem.* **2020**, *12*, 345–352.

(13) Yang, M.; Sheykhi, S.; Zhang, Y.; Milsmann, C.; Castellano, F. N. Low Power Threshold Photochemical Upconversion Using a Zirconium(IV) LMCT Photosensitizer. *Chem. Sci.* **2021**, *12*, 9069–9077.

(14) Dunlop, D.; Večeřa, M.; Gyepes, R.; Kubát, P.; Lang, K.; Horáček, M.; Pinkas, J.; Šimková, L.; Liška, A.; Lamač, M. Luminescent Cationic Group 4 Metallocene Complexes Stabilized by Pendant N-Donor Groups. *Inorg. Chem.* **2021**, *60*, 7315–7328.

(15) Pal, A. K.; Li, C.; Hanan, G. S.; Zysman-Colman, E. Blue-Emissive Cobalt(III) Complexes and Their Use in the Photocatalytic Trifluoromethylation of Polycyclic Aromatic Hydrocarbons. *Angew. Chem., Int. Ed.* **2018**, *57*, 8027–8031.

(16) Kaufhold, S.; Rosemann, N. W.; Chábera, P.; Lindh, L.; Bolaño Losada, I.; Uhlig, J.; Pascher, T.; Strand, D.; Wärnmark, K.; Yartsev, A.; Persson, P. Microsecond Photoluminescence and Photoreactivity of a Metal-Centered Excited State in a Hexacarbene–Co(III) Complex. *J. Am. Chem. Soc.* **2021**, *143*, 1307–1312.

(17) Otto, S.; Grabolle, M.; Foerster, C.; Kreitner, C.; Resch-Genger, U.; Heinze, K. $[Cr(ddpd)_2]^{3+}$: A Molecular, Water-Soluble, Highly NIR-Emissive Ruby Analogue. *Angew. Chem., Int. Ed.* **2015**, *54*, 11572–11576.
(18) Buldt, L. A.; Guo, X.; Vogel, R.; Prescimone, A.; Wenger, O. S. A Tris(Diisocyanide)Chromium(0) Complex Is a Luminescent Analog of Fe(2,2'-Bipyridine)$_3^{2+}$. *J. Am. Chem. Soc.* **2017**, *139*, 985–992.
(19) Jiménez, J.-R.; Doistau, B.; Cruz, C. M.; Besnard, C.; Cuerva, J. M.; Campaña, A. G.; Piguet, C. Chiral Molecular Ruby $[Cr(dqp)_2]^{3+}$ with Long-Lived Circularly Polarized Luminescence. *J. Am. Chem. Soc.* **2019**, *141*, 13244–13252.
(20) Wenger, O. S. Is Iron the New Ruthenium? *Chem. - Eur. J.* **2019**, *25*, 6043–6052.
(21) Caspar, J. V.; Meyer, T. J. Photochemistry of Tris(2,2'-Bipyridine)Ruthenium(2+) Ion ($Ru(bpy)_3^{2+}$). Solvent Effects. *J. Am. Chem. Soc.* **1983**, *105*, 5583–5590.
(22) Zhang, W.; Alonso-Mori, R.; Bergmann, U.; Bressler, C.; Chollet, M.; Galler, A.; Gawelda, W.; Hadt, R. G.; Hartsock, R. W.; Kroll, T.; Kjær, K. S.; Kubiček, K.; Lemke, H. T.; Liang, H. W.; Meyer, D. A.; Nielsen, M. M.; Purser, C.; Robinson, J. S.; Solomon, E. I.; Sun, Z.; Sokaras, D.; van Driel, T. B.; Vankó, G.; Weng, T.-C.; Zhu, D.; Gaffney, K. J. Tracking Excited-State Charge and Spin Dynamics in Iron Coordination Complexes. *Nature* **2014**, *509*, 345–348.
(23) Kjær, K. S.; Van Driel, T. B.; Harlang, T. C. B.; Kunnus, K.; Biasin, E.; Ledbetter, K.; Hartsock, R. W.; Reinhard, M. E.; Koroidov, S.; Li, L.; Laursen, M. G.; Hansen, F. B.; Vester, P.; Christensen, M.; Haldrup, K.; Nielsen, M. M.; Dohn, A. O.; Pápai, M. I.; Møller, K. B.; Chabera, P.; Liu, Y.; Tatsuno, H.; Timm, C.; Jarenmark, M.; Uhlig, J.; Sundstöm, V.; Wärnmark, K.; Persson, P.; Németh, Z.; Szemes, D. S.; Bajnóczi, É.; Vankó, G.; Alonso-Mori, R.; Glownia, J. M.; Nelson, S.; Sikorski, M.; Sokaras, D.; Canton, S. E.; Lemke, H. T.; Gaffney, K. J. Finding Intersections between Electronic Excited State Potential Energy Surfaces with Simultaneous Ultrafast X-Ray Scattering and Spectroscopy. *Chem. Sci.* **2019**, *10*, 5749–5760.
(24) Pyykko, P. Relativistic Effects in Structural Chemistry. *Chem. Rev.* **1988**, *88*, 563–594.
(25) Kaupp, M. The Role of Radial Nodes of Atomic Orbitals for Chemical Bonding and the Periodic Table. *J. Comput. Chem.* **2007**, *28*, 320–325.
(26) McCusker, J. K. Electronic Structure in the Transition Metal Block and Its Implications for Light Harvesting. *Science* **2019**, *363*, 484–488.
(27) Liu, Y.; Persson, P.; Sundström, V.; Wärnmark, K. Fe N-Heterocyclic Carbene Complexes as Promising Photosensitizers. *Acc. Chem. Res.* **2016**, *49*, 1477–1485.
(28) Chábera, P.; Kjaer, K. S.; Prakash, O.; Honarfar, A.; Liu, Y.; Fredin, L. A.; Harlang, T. C. B.; Lidin, S.; Uhlig, J.; Sundström, V.; Lomoth, R.; Persson, P.; Wärnmark, K. FeII Hexa N-Heterocyclic Carbene Complex with a 528 Ps Metal-to-Ligand Charge-Transfer Excited-State Lifetime. *J. Phys. Chem. Lett.* **2018**, *9*, 459–463.
(29) Chábera, P.; Liu, Y.; Prakash, O.; Thyrhaug, E.; Nahhas, A. E.; Honarfar, A.; Essén, S.; Fredin, L. A.; Harlang, T. C. B.; Kjær, K. S.; Handrup, K.; Ericson, F.; Tatsuno, H.; Morgan, K.; Schnadt, J.; Häggström, L.; Ericsson, T.; Sobkowiak, A.; Lidin, S.; Huang, P.; Styring, S.; Uhlig, J.; Bendix, J.; Lomoth, R.; Sundström, V.; Persson, P.; Wärnmark, K. A Low-Spin Fe(III) Complex with 100-Ps Ligand-to-Metal Charge Transfer Photoluminescence. *Nature* **2017**, *543*, 695–699.
(30) Kjær, K. S.; Kaul, N.; Prakash, O.; Chábera, P.; Rosemann, N. W.; Honarfar, A.; Gordivska, O.; Fredin, L. A.; Bergquist, K.-E.; Häggström, L.; Ericsson, T.; Lindh, L.;

Yartsev, A.; Styring, S.; Huang, P.; Uhlig, J.; Bendix, J.; Strand, D.; Sundström, V.; Persson, P.; Lomoth, R.; Wärnmark, K. Luminescence and Reactivity of a Charge-Transfer Excited Iron Complex with Nanosecond Lifetime. *Science* **2019**, *363*, 249–253.
(31) Winkler, J. R.; Creutz, C.; Sutin, N. Solvent Tuning of the Excited-State Properties of (2,2'-Bipyridine)Tetracyanoferrate(II): Direct Observation of a Metal-to-Ligand Charge-Transfer Excited State of Iron(II). *J. Am. Chem. Soc.* **1987**, *109*, 3470–3471.
(32) Vittardi, S. B.; Magar, R. T.; Schrage, B. R.; Ziegler, C. J.; Jakubikova, E.; Rack, J. J. Evidence for a Lowest Energy 3MLCT Excited State in $[Fe(tpy)(CN)_3]^-$. *Chem. Commun.* **2021**, *57*, 4658–4661.
(33) Kunnus, K.; Li, L.; Titus, C. J.; Lee, S. J.; Reinhard, M. E.; Koroidov, S.; Kjær, K. S.; Hong, K.; Ledbetter, K.; Doriese, W. B.; O'Neil, G. C.; Swetz, D. S.; Ullom, J. N.; Li, D.; Irwin, K.; Nordlund, D.; Cordones, A. A.; Gaffney, K. J. Chemical Control of Competing Electron Transfer Pathways in Iron Tetracyano-Polypyridyl Photosensitizers. *Chem. Sci.* **2020**, *11*, 4360–4373.
(34) Shepard, S. G.; Fatur, S. M.; Rappe, A. K.; Damrauer, N. H. Highly Strained Iron(II) Polypyridines: Exploiting the Quintet Manifold To Extend the Lifetime of MLCT Excited States. *J. Am. Chem. Soc.* **2016**, *138*, 2949–2952.
(35) Paulus, B. C.; Adelman, S. L.; Jamula, L. L.; McCusker, J. K. Leveraging Excited-State Coherence for Synthetic Control of Ultrafast Dynamics. *Nature* **2020**, *582*, 214–218.
(36) Mukherjee, S.; Torres, D. E.; Jakubikova, E. HOMO Inversion as a Strategy for Improving the Light-Absorption Properties of Fe(II) Chromophores. *Chem. Sci.* **2019**, *8*, 8115–8126.
(37) Braun, J. D.; Lozada, I. B.; Kolodziej, C.; Burda, C.; Newman, K. M. E.; van Lierop, J.; Davis, R. L.; Herbert, D. E. Iron(II) Coordination Complexes with Panchromatic Absorption and Nanosecond Charge-Transfer Excited State Lifetimes. *Nat. Chem.* **2019**, *11*, 1144–1150.
(38) Braun, J. D.; Lozada, I. B.; Herbert, D. E. In Pursuit of Panchromatic Absorption in Metal Coordination Complexes: Experimental Delineation of the HOMO Inversion Model Using Pseudo-Octahedral Complexes of Diarylamido Ligands. *Inorg. Chem.* **2020**, *59*, 17746–17757.
(39) Betley, T. A.; Qian, B. A.; Peters, J. C. Group VIII Coordination Chemistry of a Pincer-Type Bis(8-Quinolinyl)Amido Ligand. *Inorg. Chem.* **2008**, *47*, 11570–11582.
(40) Brown, A. M.; McCusker, C. E.; McCusker, J. K. Spectroelectrochemical Identification of Charge-Transfer Excited States in Transition Metal-Based Polypyridyl Complexes. *Dalton Trans.* **2014**, *43*, 17635–17646.
(41) Braun, J. D.; Lozada, I. B.; Shepit, M.; van Lierop, J.; Herbert, D. E. Pseudo-Octahedral Nickel(II) Complexes of Strongly Absorbing Benzannulated Pincer-Type Amido Ligands: Ligand-Based Redox and Non-Aufbau Electronic Behaviour. *RSC Adv.* **2021**, *11*, 3547–3555.
(42) Bridgeman, A. J.; Cavigliasso, G.; Ireland, L. R.; Rothery, J. The Mayer Bond Order as a Tool in Inorganic Chemistry. *J. Chem. Soc., Dalton Trans.* **2001**, 2095–2108.
(43) Dixon, I. M.; Khan, S.; Alary, F.; Boggio-Pasqua, M.; Heully, J.-L. Probing the Photophysical Capability of Mono and Bis(Cyclometallated) Fe(II) Polypyridine Complexes Using Inexpensive Ground State DFT. *Dalton Trans.* **2014**, *43*, 15898–15905.
(44) Zhang, K.; Ash, R.; Girolami, G. S.; Vura-Weis, J. Tracking the Metal-Centered Triplet in Photoinduced Spin Crossover of $Fe(phen)_3^{2+}$ with Tabletop Femtosecond M-Edge X-Ray

Absorption Near-Edge Structure Spectroscopy. *J. Am. Chem. Soc.* **2019**, *141*, 17180–17188.
(45) Juban, E. A.; Smeigh, A. L.; Monat, J. E.; McCusker, J. K. Ultrafast Dynamics of Ligand-Field Excited States. *Coord. Chem. Rev.* **2006**, *250*, 1783–1791.
(46) Wasinger, E. C.; de Groot, F. M. F.; Hedman, B.; Hodgson, K. O.; Solomon, E. I. L-Edge X-Ray Absorption Spectroscopy of Non-Heme Iron Sites: Experimental Determination of Differential Orbital Covalency. *J. Am. Chem. Soc.* **2003**, *125*, 12894–12906.
(47) Jay, R. M.; Eckert, S.; Fondell, M.; Miedema, P. S.; Norell, J.; Pietzsch, A.; Quevedo, W.; Niskanen, J.; Kunnus, K.; Föhlisch, A. The Nature of Frontier Orbitals under Systematic Ligand Exchange in (Pseudo-)Octahedral Fe(II) Complexes. *Phys. Chem. Chem. Phys.* **2018**, *20*, 27745–27751.
(48) Hocking, R. K.; Wasinger, E. C.; de Groot, F. M. F.; Hodgson, K. O.; Hedman, B.; Solomon, E. I. Fe L-Edge XAS Studies of $K_4[Fe(CN)_6]$ and $K_3[Fe(CN)_6]$: A Direct Probe of Back-Bonding. *J. Am. Chem. Soc.* **2006**, *128*, 10442–10451.
(49) Hahn, A. W.; Van Kuiken, B. E.; Chilkuri, V. G.; Levin, N.; Bill, E.; Weyhermüller, T.; Nicolaou, A.; Miyawaki, J.; Harada, Y.; DeBeer, S. Probing the Valence Electronic Structure of Low-Spin Ferrous and Ferric Complexes Using 2p3d Resonant Inelastic X-Ray Scattering (RIXS). *Inorg. Chem.* **2018**, *57*, 9515–9530.
(50) Kunnus, K.; Zhang, W.; Delcey, M. G.; Pinjari, R. V.; Miedema, P. S.; Schreck, S.; Quevedo, W.; Schröder, H.; Föhlisch, A.; Gaffney, K. J.; Lundberg, M.; Odelius, M.; Wernet, P. Viewing the Valence Electronic Structure of Ferric and Ferrous Hexacyanide in Solution from the Fe and Cyanide Perspectives. *J. Phys. Chem. B* **2016**, *120*, 7182–7194.
(51) de Groot, F. M. F. Ligand and Metal X-Ray Absorption in Transition Metal Complexes. *Inorg. Chim. Acta* **2008**, *361*, 850–856.
(52) Baker, M. L.; Mara, M. W.; Yan, J. J.; Hodgson, K. O.; Hedman, B.; Solomon, E. I. K- and L-Edge X-Ray Absorption Spectroscopy (XAS) and Resonant Inelastic X-Ray Scattering (RIXS) Determination of Differential Orbital Covalency (DOC) of Transition Metal Sites. *Coord. Chem. Rev.* **2017**, *345*, 182–208.
(53) Wu, J.; Alías, M.; de Graaf, C. Controlling the Lifetime of the Triplet MLCT State in Fe (II) Polypyridyl Complexes through Ligand Modification. *Inorganics* **2020**, *8*, 16.
(54) Shimura, Y.; Tsuchida, R. Absorption Spectra of Co (III) Complexes. II. Redetermination of the Spectrochemical Series. *Bull. Chem. Soc. Jpn.* **1956**, *29*, 311–316.
(55) Carey, M. C.; Adelman, S. L.; McCusker, J. K. Insights into the Excited State Dynamics of Fe(II) Polypyridyl Complexes from Variable-Temperature Ultrafast Spectroscopy. *Chem. Sci.* **2019**, *10*, 134–144.
(56) Paulus, B. C.; Nielsen, K. C.; Tichnell, C. R.; Carey, M. C.; McCusker, J. K. A Modular Approach to Light Capture and Synthetic Tuning of the Excited-State Properties of Fe(II)-Based Chromophores. *J. Am. Chem. Soc.* **2021**, *143*, 8086–8098.

TOC Graphic